ECOLOGY

Enhanced causal effect of ecosystem photosynthesis on respiration during heatwaves

Jiaye Ping[1,2], Erqian Cui[1,2], Ying Du[1,2], Ning Wei[1,2], Jian Zhou[1,3], Jing Wang[1,2], Shuli Niu[4], Yiqi Luo[3], Jianyang Xia[1,2]*

Because of global warming, Earth's ecosystems have been experiencing more frequent and severe heatwaves. Heatwaves are expected to tip terrestrial carbon sequestration by elevating ecosystem respiration and suppressing gross primary productivity (GPP). Here, using the convergent cross-mapping technique, this study detected positive bidirectional causal effects between GPP and respiration in two unprecedented European heatwaves. Heatwaves enhanced the causal effect strength of GPP on respiration rather than respiration on GPP across 40 site-years of observations. Further analyses and global simulations revealed spatial heterogeneity in the heatwave response of the causal link strength between GPP and respiration, which was jointly driven by the local climate and vegetation properties. However, the causal effect strength of GPP on respiration showed considerable uncertainties in CMIP6 models. This study reveals an enhanced causal link strength between GPP and respiration during heatwaves, shedding light on improving projections for terrestrial carbon sink dynamics under future climate extremes.

INTRODUCTION

Terrestrial ecosystems can mitigate climate change by absorbing approximately one-third of anthropogenic carbon (C) emissions (*1*). Such a global land net C sink stems from higher gross primary productivity (GPP) than ecosystem respiration (Re). However, in recent decades, the number of abnormal high-temperature events over global lands, e.g., heatwaves, has been increasing in both frequency and intensity (*2*–*5*). It is still unclear whether heatwaves will quickly threaten the global land C sink and even trigger a widespread transition of terrestrial ecosystems from C sinks to sources.

Because temperature regulates the majority of metabolic processes in the biosphere, both photosynthetic and respiratory rates are temperature dependent in terrestrial ecosystems. The different responses of GPP and Re to temperature, especially at high temperatures, can determine the impact of heatwaves on ecosystem C sink. As the temperature rises, the leaf-level photosynthetic rate increases until the temperature exceeds its thermal optima, which is estimated to be 23° ± 6°C (*6*, *7*). High temperature during heatwaves can significantly down-regulate GPP by triggering changes in leaf-level processes, including reducing Rubisco activity and electron transport (*8*), altering leaf thickness and age (*9*, *10*), and stimulating stomatal closure with amplified vapor pressure deficit (VPD) (*11*). On the ecosystem scale, heatwaves can inhibit GPP by reshaping canopy architectures (*12*), microclimate buffering capacity (*13*), and phenology (*14*). As opposed to GPP, Re increases exponentially with rising temperature (*15*). However, contrary to GPP, previous studies have documented either increasing (*16*–*18*) or decreasing (*19*–*21*) Re during heatwaves. Hence, it remains unclear how the balance between GPP and Re (i.e., ecosystem C sink) changes in extremely high temperatures (e.g., heatwave events).

Three hypotheses can be formulated to characterize the heatwave impacts on ecosystem C sink due to different causal relationships between GPP and Re. The first hypothesis assumes that GPP declines as Re rises during heatwaves (*16*). This divergence of temperature dependence between GPP and Re elicits a quick reversal of the ecosystem C balance from sink to a source (i.e., hypothesis I in Fig. 1A). This hypothesis supposes no causal relationship between GPP and Re during heatwaves. A growing body of evidence has shown that Re can be decoupled from GPP through nonstructural carbohydrates (NSCs) fluctuations. NSCs mainly encompass soluble sugars and starch, serving as an accessible energy reserve pool that buffers the asynchrony of C supply (photosynthesis) and metabolism demand (i.e., respiration and growth) (*22*). For example, photosynthesis is ceased by high temperatures or drought, while NSC reserves supply substrate to enable increased respiration (*23*–*25*). However, reduced GPP due to high temperatures may fail to replenish the NSC storage pool that is required for Re, causing a decline in Re. Thus, as illustrated in Fig. 1, the second hypothesis assumes a unidirectional causal effect of GPP on Re during heatwaves, leading to a lagged transition of ecosystem C sink to the source (i.e., hypothesis II in Fig. 1A). Our third hypothesis assumes a bidirectional causality between GPP and Re during heatwaves (i.e., hypothesis III in Fig. 1A). Consistent with this third hypothesis, some experimental studies have shown that climate warming can stimulate plant respiration and depletion of NSCs at night, leading to a compensatory increase in photosynthesis during the following day (*26*, *27*). In contrast, low plant respiratory rates associated with excessive NSC storage may impair chloroplast function or restrict CO_2 diffusion to down-regulate photosynthesis (*28*, *29*). Recently, numerous flux tower measurements have shown parallel declines in GPP and Re during heatwaves (*19*–*21*, *30*, *31*), supporting hypotheses II and III rather than hypothesis I. Some land-surface models have already considered

[1]Zhejiang Tiantong Forest Ecosystem National Observation and Research Station, State Key Laboratory of Estuarine and Coastal Research, School of Ecological and Environmental Sciences, East China Normal University, Shanghai 200241, China. [2]Research Center for Global Change and Complex Ecosystems, Institute of Eco-Chongming, East China Normal University, Shanghai 200241, China. [3]School of Integrative Plant Science, College of Agriculture and Life Sciences, Cornell University, Ithaca, NY, 14850, USA. [4]Key Laboratory of Ecosystem Network Observation and Modeling, Institute of Geographic Sciences and Natural Resources Research, Chinese Academy of Sciences, Beijing 100101, China.
*Corresponding author. Email: jyxia@des.ecnu.edu.cn

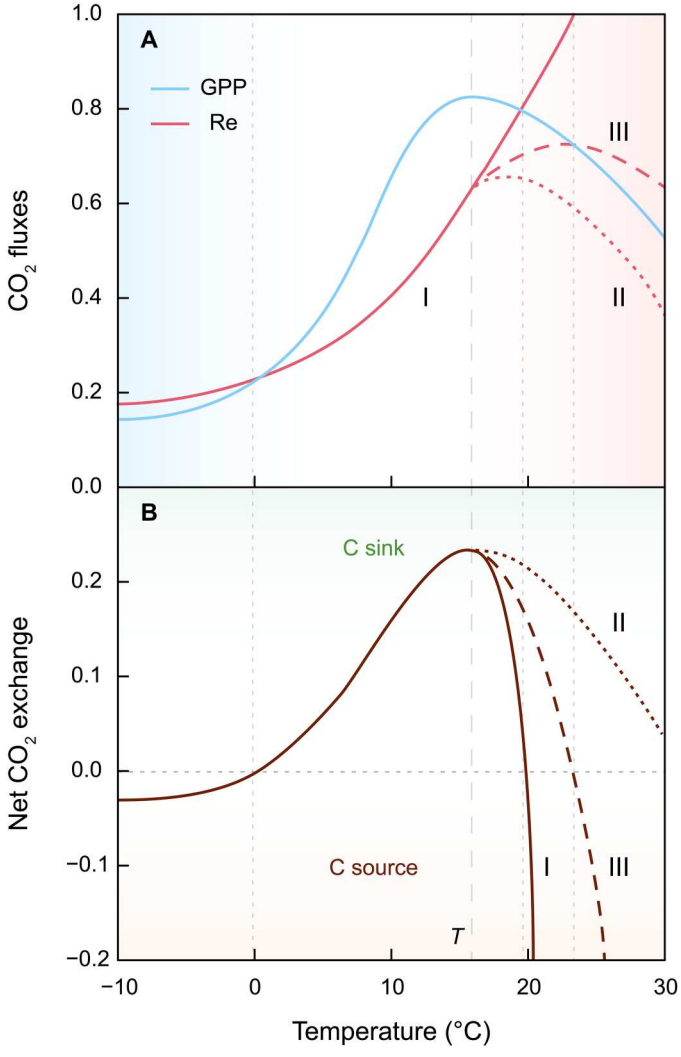

Fig. 1. Schematic diagram for the theoretical temperature dependence curve of CO_2 fluxes and net CO_2 exchange. (**A**) Photosynthesis (GPP) and ecosystem respiration (Re). (**B**) Net ecosystem exchange (NEE). Hypothesis I represents the kinetic sensitivity of Re independent with the causal effect of GPP. Hypothesis II represents a unidirectional causality from GPP to Re. Hypothesis III represents a bidirectional causal relationship between GPP and Re. Here is a sign convention where both fluxes are defined to be positive. C, carbon.

NSCs to buffer the imbalance between GPP and C depletion activities (i.e., respiration and growth) (*25*). Thus, detecting the causal relationships between GPP and Re and their response to heatwave is critical for improving our understanding of ecosystem C sink dynamics in extreme climatic events.

With the rapid progress in the fields of computer science, physics, and statistics, several observational causal inference methods from time series have been developed to infer the causal link strength in Earth's system (*32*–*35*). Among them, there is a powerful methodological approach called "convergent cross-mapping" (CCM). On the basis of Takens' theorem and nonlinear state-space reconstruction (*33*, *36*), CCM detects causal link strength between paired observations by measuring the extent to which the affected variable can reliably estimate the states of the causal variable (termed "cross-mapping skill," ρ; Materials and Methods). Recently, CCM has been widely applied to study the causal feedback between temperature variability and greenhouse gas concentrations (*37*), the biodiversity-mediated causal networks in aquatic ecosystems (*38*), the causal effect of global atmospheric CO_2 on Mediterranean vegetation dynamics (*39*), and the time-varying interaction network of natural fish community (*40*).

In this study, we examined the strength of the GPP-Re causality and its shifts during heatwaves. We also applied the CCM method for two record-breaking European heatwave events in 2003 and 2018. The observations of eddy covariance fluxes, including 40 site-years (table S1), were analyzed to quantify the changes in the GPP-Re causality strength during the heatwaves. All of the available climatological and hydrological factors, their differences between heatwave and normal periods, and some static variables such as plant functional type (PFT) (table S2) were used to identify the drivers of spatial heterogeneity in the strength of the causal linkage using redundancy analysis (RDA). CCM is also applied to reveal the factors that mediate the underlying causal mechanisms between GPP and Re. Furthermore, a summer heatwave experiment in the Northern Hemisphere was conducted in the Community Earth System Model Version 2 (CESM2) to determine the causal effect strength of simulated GPP on simulated Re by increasing the forcing temperature from 0° to 4°C, aiming to investigate CESM2's ability to capture the heatwave response of this causal relationship. Moreover, we applied CCM to 11 Coupled Model Intercomparison Project Phase 6 (CMIP6) models in the causal relationship between GPP and Re, particularly splitting the Re into the autotrophic respiration (Ra) and the heterotrophic respiration (Rh).

RESULTS AND DISCUSSION

Causal analysis between GPP and Re

Before the 2003 and 2018 European heatwave events, the flux tower observations showed that GPP and Re followed saturating functions in normal years (Fig. 2A). This is in line with the fact that the current climate is generally below the tipping point of the ecosystem C sink (*16*). During the heatwaves, the rates of photosynthetic CO_2 uptake and respiratory CO_2 release also increased with the temperature and declined after reaching their maximum values (Fig. 2B). Although the temperature at which GPP and Re began to decline varied from site to site, there was a net C uptake period in the intermediate temperature range. The observations also showed a downward trend of Re during heatwaves (Fig. 2B and fig. S1), which supports the pattern of parallel declines in GPP and Re in hypotheses II and III but not hypothesis I (Fig. 1A). Across 2003 and 2018, the heatwaves caused significant reductions in GPP (i.e., from 9.26 ± 0.87 to 8.21 ± 1.61 g C m^{-2} day^{-1}; means ± SD, $P < 0.01$) and Re (i.e., from 6.22 ± 0.36 to 5.62 ± 0.52 g C m^{-2} day^{-1}, $P < 0.01$) in summer. In addition, the net ecosystem productivity (NEP) over the 40 site-years showed no significant change in summer (i.e., from 3.05 ± 2.06 to 2.59 ± 1.66 g C m^{-2} day^{-1}, $P = 0.28$) (fig. S2), as a result of the decrease of both GPP and Re.

We then applied CCM on the time series of GPP and Re data using a nonlinear state-space reconstruction method through lagged coordinate embedding (Fig. 2, C and D). A daily time distance between adjacent coordinates is used as the time lag to create a multidimensional representation of the system's dynamics

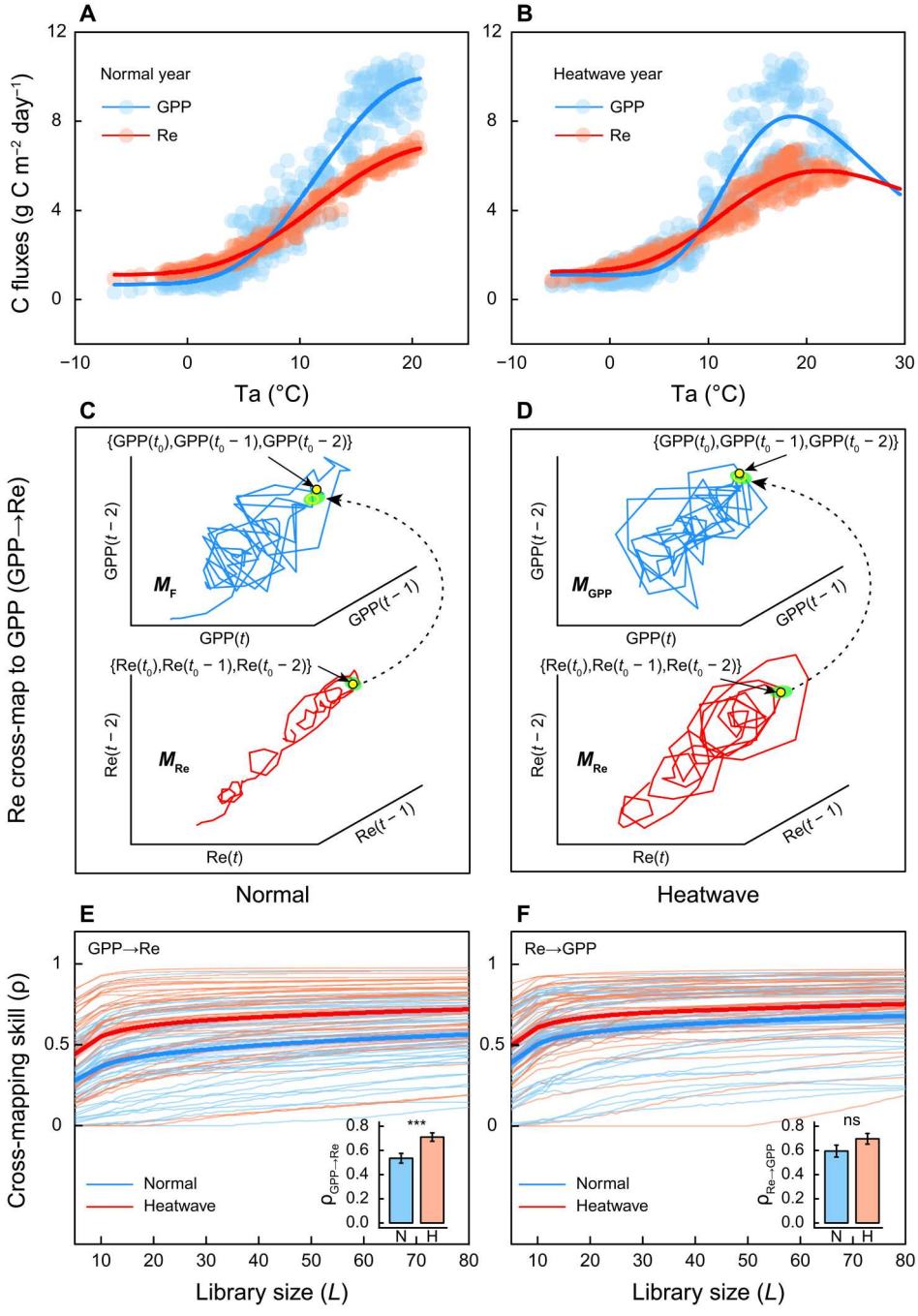

Fig. 2. Observational GPP and Re with air temperature and the application of CCM. (**A**) Sensitivity of GPP and Re to air temperature in normal years. C, carbon. (**B**) Sensitivity of GPP and Re to air temperature during heatwave years. (**C**) CCM test for summer GPP→Re from shadow manifolds $\boldsymbol{M_{Re}}$ to $\boldsymbol{M_{GPP}}$ of normal years. For clear visualization, here take the site FI-Var for example, the embedding dimension $E = 3$. For each site, E is selected on the basis of the optimal cross-mapping skill (figs. S14 and S15). The solid yellow circles on $\boldsymbol{M_{GPP}}$ and $\boldsymbol{M_{Re}}$ are the contemporaneous lagged coordinate vectors at time t_0, i.e., $\boldsymbol{GPP(t_0)}$ and $\boldsymbol{Re(t_0)}$. The open yellow circle is the estimated result. The green ellipse on $\boldsymbol{M_{Re}}$ is the nearest neighbors of $\boldsymbol{Re(t_0)}$. The green ellipse on $\boldsymbol{M_{GPP}}$ is the point simultaneously corresponding to that of $\boldsymbol{M_{Re}}$. GPP(t), GPP(t − 1), and GPP(t − 2) are the original GPP time series without lag, with a lag of 1 day, and with a lag of 2 days, respectively. The three time-series formed a three-dimensional lagged coordinate vectors, also termed "reconstructed state space." (**D**) CCM test for summer GPP→Re from shadow manifolds M_{Re} to M_{GPP} of heatwave years. (**E**) CCM results of GPP→Re for 40 site-years in summer of normal years. Bold lines and shadows indicate the mean and SE. The inserted panel shows that $\rho_{GPP→Re}$ in the summer of normal (N) and heatwave (H) years is statistically significant ($P = 0.00054$) at the 5% level using a two-sided paired Wilcoxon signed rank test. Bar indicates the mean and the whisker shows 1 SE. (**F**) Same with (E) but for Re→GPP. "ns" represents nonsignificant with $P = 0.09691$.

(figs. S3 and S4 and Materials and Methods). A bidirectional causal relationship between GPP and Re under heatwaves was quantified (Fig. 2, E and F), which supports hypothesis III (Fig. 1). The level to which predictive power converges (i.e., cross-mapping skill: $\rho_{GPP\rightarrow Re}$ and $\rho_{Re\rightarrow GPP}$) was regarded as an estimator of the causal link strength between GPP and Re in each site-year. The bidirectional causality strength between GPP and Re varied among sites (fig. S5). Across all sites, heatwaves significantly increased the causal effect strength of GPP on Re ($\rho_{GPP\rightarrow Re}$) from 0.54 ± 0.04 to 0.71 ± 0.03 (means ± SE, $P < 0.001$; Fig. 2E), but not for the opposite causal link of $\rho_{Re\rightarrow GPP}$ ($P > 0.05$; Fig. 2F).

Associated with the enhanced causal effect strength of GPP on Re ($\Delta\rho_{GPP\rightarrow Re}$), not only the correlation coefficient (R) but also the slope (K) of the linear relationship between GPP and Re increased during the heatwaves (fig. S6). As a result, heatwaves reduce not only GPP but also Re in most sites, leading to an unchanged NEP between the normal and heatwave years across all sites (fig. S2). These results indicate an increased resistance of ecosystem C sink to heatwaves due to the enhanced causal effect strength of GPP on Re (Fig. 1). A recent analysis predicted an occurrence of the temperature tipping point of the terrestrial biosphere within the next two to three decades if Re exponentially rises with the increase in temperature (*16*). However, our findings suggest that the causal effect of GPP on Re would allow for reduced Re under future climate extremes. Therefore, the enhanced causal effect strength of GPP on Re could be a critical mechanism for the rise in the temperature tipping point in some terrestrial ecosystems.

Mechanisms of causality between GPP and Re

We further conducted an RDA to locate the major factors that drove the $\Delta\rho_{GPP\rightarrow Re}$ during the heatwaves (table S2). The RDA found that the enhanced $\rho_{GPP\rightarrow Re}$ in the heatwaves was positively correlated with VPD, air temperature (Ta), and heatwave-induced changes in VPD (ΔVPD) (Fig. 3A). A relative importance method was performed to quantify the contributions of these factors to the spatial variations in $\Delta\rho_{GPP\rightarrow Re}$ among the sites. This method measured how much each predictor, relative to the other predictors, contributed to explaining the variation in $\Delta\rho_{GPP\rightarrow Re}$ by ranking the predictors in terms of their contributions. The results showed that the mean air temperature was the most influential factor, with 15.23% contributions to the spatial heterogeneity in $\Delta\rho_{GPP\rightarrow Re}$. The heatwave-induced changes in VPD (ΔVPD) and soil water content (ΔSWC) together explained 20.08%. The vegetation properties also explained a considerable part of the heterogeneity next to climatic drivers. For example, PFT and leaf area index (LAI) together explained 20.75% of the spatial heterogeneity in $\Delta\rho_{GPP\rightarrow Re}$ (Fig. 3B). These results suggest that the causality between GPP and Re is a complex nonlinear interaction affected by multiple factors such as the heatwave-induced changes in climatic factors (i.e., ΔVPD and ΔSWC), local climate, and vegetation properties.

Across the 40 sites, most sites experienced increasing VPD and decreasing SWC during heatwaves (fig. S7, F and G). However, heatwaves reduced VPD at the sites of IT-SR2, CZ-BK1, CZ-Stn, CZ-Lnz, and RU-Fyo but increased SWC at the sites of FR-Bil, DE-RuW, CZ-Stn, IT-SR2, CH-Lae, and NL-Loo. The mean $\Delta\rho_{GPP\rightarrow Re}$ was 0.08 and 0.12 across the five sites with reducing VPD and the six sites with increasing SWC, respectively, both of which were smaller than the average of $\Delta\rho_{GPP\rightarrow Re}$ across all sites (0.14). These results support the relative importance analysis that ΔSWC and ΔVPD were the two major response variables to explain the positive heatwave effect on $\rho_{GPP\rightarrow Re}$ (Fig. 3B).

We then applied CCM with a more detailed causal path to understanding the causality strength changes between GPP and Re during heatwaves. To exclude the potential spurious effects of GPP and Re from net ecosystem exchange (NEE)–based constructs, we used the daytime NEE dominated by GPP and the nighttime NEE that only consists of nighttime Re in this analysis. We showed the paths by which the causal link strength significantly increased during heatwaves (Fig. 3C). The results based on NEE measurements detected bidirectional causal effects between daytime and nighttime NEE (Fig. 3c), which supported Hypothesis III (Fig. 1). The bidirectional causal link strength between Re and GPP could be potentially explained by the effects of NSCs on GPP. Several models have attempted to explain the causal link between Re (or NSCs) and GPP. For example, studies based on an optimal stomatal model have suggested that excess NSCs directly down-regulate GPP via coordinating stomatal closure (*41*, *42*). An alternative model (*43*) has indicated that increasing demand for

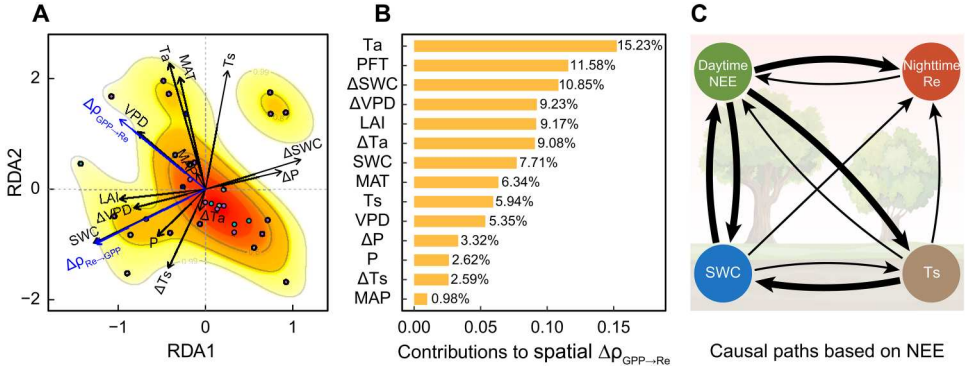

Fig. 3. Spatial contributions to the enhanced causal effect strength of GPP on Re. (**A**) RDA. Projection of response and explanatory variables and sites on the plane defined by RDA axes 1 and 2. RDA triplot ordinates the sites as points, whose PFT was marked with colors, while both the response variables, $\Delta\rho_{GPP\rightarrow Re}$ and $\Delta\rho_{Re\rightarrow GPP}$ (blue vectors), and the explanatory variables (black vectors) as vectors. Scores are scaled by the square root of the eigenvalues. Color map defines the kernel density of the sites' distribution. (**B**) Relative importance analysis of the explanatory variables to the spatial variations in $\Delta\rho_{GPP\rightarrow Re}$. (**C**) Causal paths that SWC and soil temperature (Ts) mediate the causal relationship between daytime NEE and nighttime Re during heatwaves. The solid arrows indicate causal links among daytime NEE, nighttime NEE, SWC, and Ts. Arrow thickness indicates the link with a significant increase in the causal strength (i.e., converged cross-mapping skill, ρ) during heatwaves ($P < 0.05$).

NSCs to sustain Re can cause stomata to open and thus stimulate GPP. Besides, heatwaves increased the causal effect strength of daytime on nighttime NEE from 0.16 ± 0.04 to 0.35 ± 0.06 (means ± SE, $P = 0.019$), but not the causal effect strength of nighttime on daytime NEE (Fig. 3C). This result is consistent with the causal relationship between GPP and Re (Fig. 2, E and F). The enhanced causal effect strength of daytime on nighttime NEE can be explained by the increased bidirectional causal link strength between daytime NEE and SWC, with $\rho_{GPP \to SWC}$ and $\rho_{SWC \to GPP}$ increased from 0.28 ± 0.05 to 0.50 ± 0.05 ($P = 0.014$) and from 0.28 ± 0.06 to 0.45 ± 0.07 ($P = 0.012$), respectively. This finding indicates strengthened causal interactions between C and water processes during heatwaves (*44*).

Modeling heatwave impacts on causality between GPP and re

We conducted a simulation experiment with a widely used land-surface model, the Community Land Model Version 5 (CLM5), to evaluate the impact of heatwave events on terrestrial C sinks in the Northern Hemisphere. The model simulations were driven by the CRUNCEPv7 meteorological forcing since 2000 with appropriate initial conditions (Materials and Methods). We simulated heatwaves in the model by increasing the mean air temperature of summer (June–August) by 4°C in 2016, which was the hottest year from 1880 to 2020. The modeling results showed that heatwave events reduced the terrestrial NEP in 2016 over the Northern Hemisphere (Fig. 4, A and B). One mechanism could be the higher VPD and associated lower stomatal conductance during heatwaves (fig. S8). However, the lands in the Northern Hemisphere showed a C sink during heatwaves, even in the hottest scenario (i.e., the 4°C heatwave experiment) (fig. S9). The FLUXNET observations showed a strong spatial correlation between changes in maximum daily GPP (ΔGPP_{max}) and maximum daily Re (ΔRe_{max}) during heatwaves (Fig. 4C). Such covarying ΔRe_{max} and ΔGPP_{max} during heatwaves was captured by the model simulations (Fig. 4C). However, the slope of the linear correlation between ΔRe_{max} and ΔGPP_{max} was significantly lower in CLM5 than in the observation (*t* test, $P < 0.05$; Fig. 4C), suggesting that the temperature sensitivity of Re_{max} may be underestimated and needs improvement in the model for capturing the correct response. This lower dependence of ΔRe_{max} on ΔGPP_{max} in the model than the observation supports recent recommendations and initiatives to improve the coupling between C assimilation and vegetation C demand in the models (*25*, *45*).

We then applied CCM to the output GPP and Re from CLM5 simulations. The model simulations indicated a strong causal link strength between GPP and Re in the Northern Hemisphere (fig. S10). The causal link strength of GPP on Re ($\rho_{GPP \to Re}$) enhanced during the heatwave with ρ significantly increased from 0.747 ± 0.005 to 0.772 ± 0.004 (mean ± SE, $P < 0.001$; fig. S10C). In comparison with $\rho_{GPP \to Re}$, the causal effect strength of Re on GPP ($\rho_{Re \to GPP}$) showed a slightly less increment from 0.745 ± 0.005 to 0.763 ± 0.005 over the Northern Hemisphere ($P < 0.001$; fig. S10G). This finding is consistent with the observations that heatwave has a higher positive impact on the $\rho_{GPP \to Re}$ than $\rho_{Re \to GPP}$ (Fig. 2). However, the causal link strength of $\rho_{GPP \to Re}$ and $\rho_{Re \to GPP}$ in the normal year was higher in CLM5 than the observations (Fig. 2, E and F). Although the pool size of NSCs decreases along with the warming gradient in heatwaves in the CLM5 simulations (fig. S11), the role of NSCs in decoupling GPP and Re may need improvement in the model. The RDA analysis on the CLM5 outputs further showed that the major drivers of the spatial heterogeneity in the strength of the causal linkage $_{GPP \to Re}$ are also consistent between the model and observations. For example, the heatwave-induced change in VPD (ΔVPD), local temperature, and vegetation properties together explain >50% of the spatial heterogeneity in $\Delta\rho_{GPP \to Re}$ for both CLM simulations (Fig. 4I) and FLUXNET measurements (Fig. 3B). PFT plays an important role in driving spatial heterogeneity in the strength of the causal link ($\rho_{GPP \to Re}$). The results showed that PFT was the largest contributor to spatial variations in $\rho_{GPP \to Re}$ in both normal and heatwave years (Fig. 4, G and H). This finding is consistent with the observations (fig. S12).

Because the CLM5 is not a coupled Earth system model (ESM), the offline modeling experiment in this study ignored the transient feedback between the ecosystem and climate system during the heatwave. We further explored whether the causal link strength between GPP and Re is comparative among the state-of-the-art ESMs. By applying CCM to the extracted GPP and Re of each site in the 11 CMIP6 ESMs, we found a large uncertainty in $\rho_{GPP \to Re}$ among the models (ranging from 0.57 ± 0.12 to 0.83 ± 0.04; Fig. 5A). Taking advantage of the CMIP6 data, we split the Re into the autotrophic respiration (Ra) and the heterotrophic respiration (Rh). Then, we investigated the causal effect of GPP on Ra and Rh. The results showed that $\rho_{GPP \to Ra}$ (0.98 ± 0.04) was significantly stronger than $\rho_{GPP \to Rh}$ (0.88 ± 0.13), especially at the middle and lower latitudes in the Northern Hemisphere (Fig. 5, B and C, and fig. S13B). By explicitly considering different time lags for cross-mapping, GPP acted with significantly less time delay on Ra (0.70 ± 0.35 months) than on Rh (1.21 ± 0.45 months) (Fig. 5, E and F, and fig. S13D). We further explored how summer temperature affects GPP and Re in coupled ESMs by analyzing outputs from nine ESMs in the 1pctCO2-rad simulation in the Coupled Climate Carbon Cycle Model Intercomparison Project (C4MIP) experiments. We found that the coupled ESMs have large uncertainty in modeling the responses of GPP and Re to summer warming (Fig. 6, A and B). This uncertainty calls for more research on the direct causal effect of GPP on Ra (Fig. 5D) and the lagged causal effect of GPP on Rh (Fig. 5G) during heatwaves.

In summary, this study revealed an enhanced causal effect strength of GPP on Re in heatwave events associated with synchronous declines in GPP and Re during the heatwaves. Neither the observations nor the model simulations detected an abrupt heatwave-driven shift from C sink to source. These findings indicate that the enhanced causal link strength between GPP and Re could increase the resistance of terrestrial ecosystem C sink to extreme heatwaves. This study also found that local climate and vegetation properties jointly contributed to the spatial heterogeneity in the heatwave effect on causality strength. However, there is still considerable uncertainty in the causal impact of ecosystem photosynthesis on respiration among current ESMs. Overall, our findings show the importance of heatwaves in altering causal link strength between C processes and call for improvements in heatwave effects on terrestrial ecosystems in ESMs.

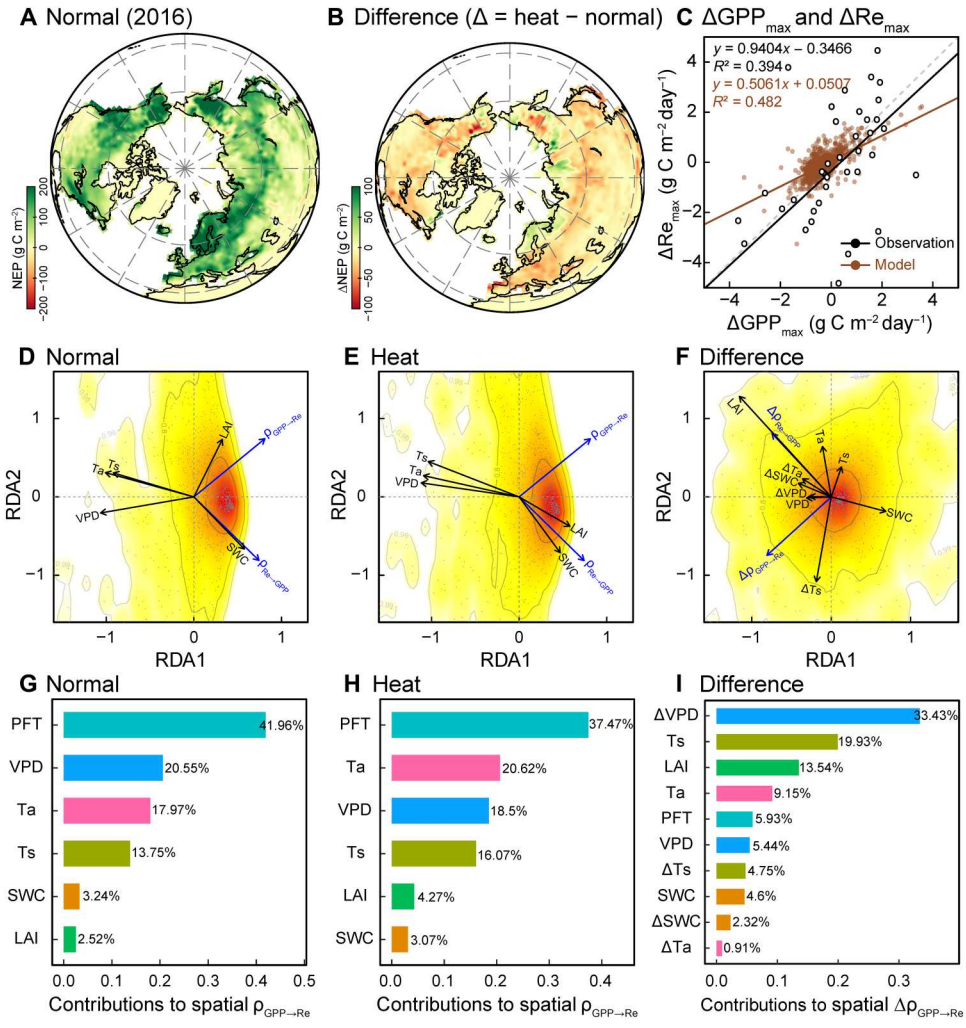

Fig. 4. CLM5 simulations and the spatial differences in the causal relationship between GPP and Re. (**A**) Total NEP in the Northern Hemisphere from June to August in 2016 with normal temperature forcing. (**B**) Difference in NEP between the hottest scenario (i.e., 4°C heatwave experiment) and the ambient scenario. (**C**) Linear relationship between the changed GPP_{max} and the changed Re_{max} by 4°C heatwave experiment simulation. (**D**) RDA of the causal relationship between GPP and Re in the default ambient simulation. (**E**) RDA of the spatial causality between GPP and Re in the heatwave simulation. (**F**) RDA for the changed causal link strength between GPP and Re during heatwaves. (**G** to **I**) Relative importance analysis of the spatial variations in the causal effect strength of GPP on Re in normal (G) and heatwave simulation (H), and that for the spatial variations in the changed causal link strength during heatwaves (I), respectively. LAI, leaf area index.

MATERIALS AND METHODS

Eddy-covariance observation

Two unprecedented European heatwave events in 2003 and 2018 were selected. The former was the hottest in Europe since at the latest 1500 CE (*46*), and the latter was the most severe during 2000–2020 (*30*). The years 2002 and 2017 were selected as reference years, referring to the "normal" year in the main text. A typical summer (June–August) of a year was chosen as heatwave-affected period to do analyses in this study. Eddy covariance flux towers have provided continuous measurements in ecosystem C and energy exchange and key meteorological data. Study sites of the 2003 European heatwave event were selected according to the analysis of Ciais *et al.* (*19*). Data are available on the European Fluxes Database Cluster (EFDC) (*47*) (www.europe-fluxdata.eu). Sites of the 2018 European heatwave are available through the Drought 2018 Team as part of the Integrated Carbon Observation System (ICOS) (*48*) (www.icos-cp.eu/data-products/YVR0-4898). Detailed site information can be found in table S1. We used the average daily GPP, Re, and explanatory data (details in table S2) from the EFDC and ICOS datasets, which were processed with a standardized set of quality control and gap-filling (*49*). The estimates of GPP and Re partitioned from NEE were filtered with Variable USTAR Threshold method using a nighttime partitioning approach. The nighttime data were used to parameterize a respiration model that was then applied to the whole dataset to estimate Re. GPP was then calculated as the difference between Re and NEE. Because of the construction of GPP and Re, we also used the direct measurements, i.e., the daytime NEE and nighttime NEE replacing the GPP and Re, respectively, to avoid the spurious effects of GPP and Re in CCM analysis. The daytime NEE and nighttime NEE are limited by the data availability on EFDC, so only the data related to the 2018 heatwave event were used in the causal analysis of daytime NEE and nighttime NEE.

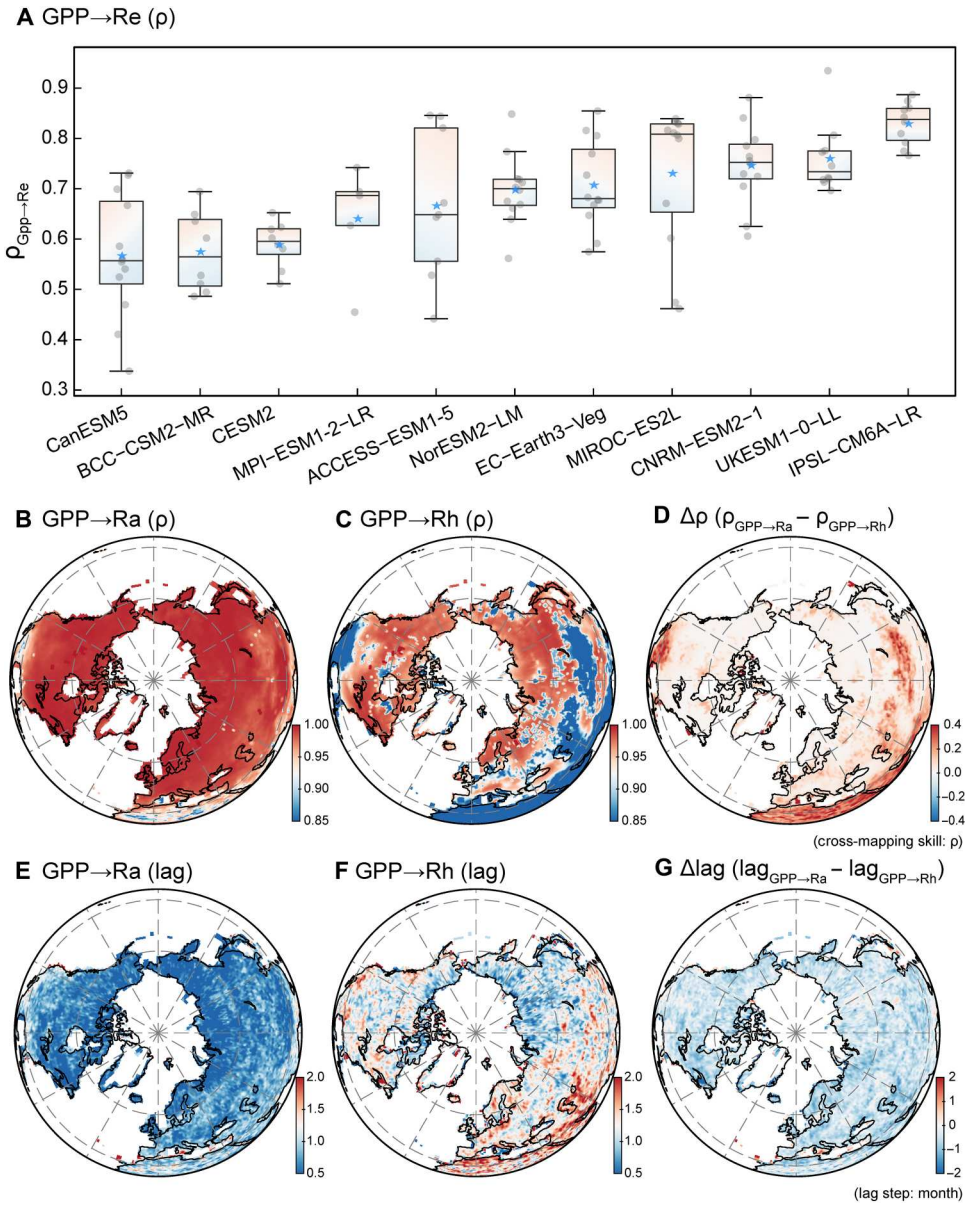

Fig. 5. Causal relationship of GPP on Ra and Rh in 11CMIP6 models. (**A**) Causal link strength of GPP on Re in CMIP6 historical simulation. The gray dots denote the sites. The star denotes the mean. The whisker denotes the 25th and 75th percentiles. (B to G) Spatial distribution of the ensemble mean of the causal effect strength of GPP on Ra and Rh in CMIP6 ESMs. (**B**) Cross-mapping skill (ρ) of the causal link GPP→Ra. (**C**) Cross-mapping skill of the causal link GPP→Rh. (**D**) Difference of the cross-mapping skill in $\rho_{GPP\to Ra}$ and $\rho_{GPP\to Rh}$. (**E**) Lag step at the optimal cross-mapping skill in the causal link GPP→Ra. (**F**) Lag step at the optimal cross-mapping skill in the causal link GPP→Rh. (**G**) Difference of the lag step in $lag_{GPP\to a}$ and $lag_{GPP\to Rh}$.

Temperature dependence curve for GPP and Re

The GPP-Ta and Re-Ta curves in Fig. 2 (A and B) are fitted using the mean of 40 site-years by a peak function

$$\begin{cases} y = y_0 + Ae^{(-e^{(-z)}-z+1)} \\ z = (x - x_c)/\omega \end{cases} \quad (1)$$

In Fig. 2A, the R^2 (coefficient of determination) is 0.93 for the GPP-Ta curve and 0.98 for the Re-Ta curve in normal years. Parameters of y_0, x_c, ω, and A in the GPP-Ta curve are 0.67 ± 0.14, 21.93 ± 0.86, 10.90 ± 0.72, and 9.30 ± 0.36, respectively, and that of the Re-Ta curve are 1.10 ± 0.06, 23.81 ± 0.61, 12.96 ± 0.51, and 5.86 ± 0.15, respectively. Both fittings are significant with $P < 0.001$. In Fig. 2B, the R^2 is 0.87 and 0.95 for the GPP-Ta curve and the Re-Ta curve during heatwave years, respectively, with parameters of y_0, x_c, ω, and A being 1.10 ± 0.11, 18.60 ± 0.34, 7.55 ± 0.38, and 7.12 ± 0.15 for GPP-Ta and that of Re-Ta being 1.26 ± 0.06, 21.63 ± 0.48, 11.27 ± 0.49, and 4.50 ± 0.09, respectively. All four curves are significantly fitted with $P < 0.001$.

Convergent cross-mapping

CCM was used to distinguish causality from spurious correlation in multivariate time series from nonlinear dynamical systems (*33*).

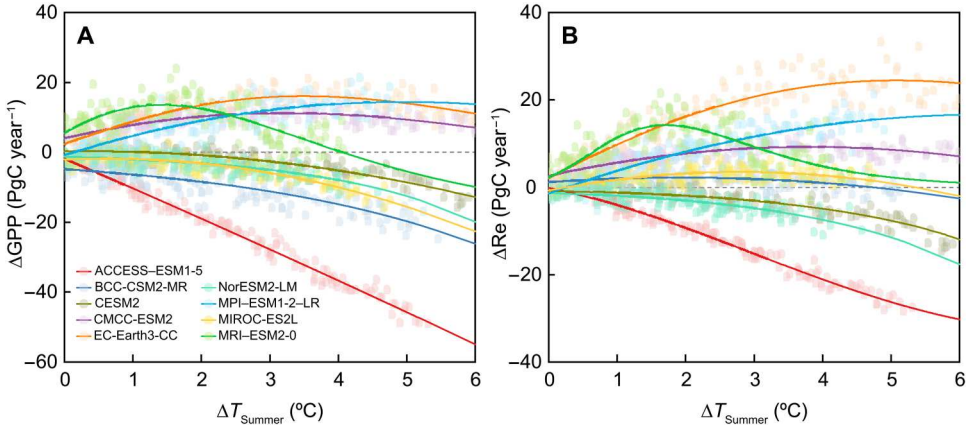

Fig. 6. Uncertainty in the summer temperature responses of GPP and Re in CMIP6 models. (**A**) Relationships between summer temperature change (ΔT_{Summer}) and GPP changes (ΔGPP) in the Northern Hemisphere in coupled Earth System Models (ESMs) by using 1pctCO2-rad simulation in the C4MIP experiments. (**B**) The relationships between ΔT_{Summer} and ΔRe in the summer of the Northern Hemisphere among ESMs. The lines denote the fitting curves. The details for the equations and the measure of fit can be found in table S6.

CCM analysis is based on nonlinear state space reconstruction through lagged coordinate embedding proved by Takens (*36*). Takens′ theorem states that in a multidimensional dynamical system with only a finite number of observable variables, the essential information of the system is retained in the time series of any observed single variable of that system. Therefore, the system dynamics can be presented in the state space by substituting the time lags of the observable time series for the unknown variables with Takens′ theorem and its extensions (*50*). Effectively, if variable *X* causes *Y*, then causality can be expected if states of the causal variable *X* can be reliably recovered from the affected time series history of *Y* (i.e., cross-mapping). The estimation skill is quantified by calculating the correlation coefficient (cross-mapping skill, ρ) between the predicted and observed value of *X*. The level to which the predictive power converges can be considered as an estimator of the causal link strength. One of the corollaries of Takens′ theorem is that multiple reconstructions map not only to the original dynamic system but also to each other.

We applied CCM to quantify causal interactions between pairs of time series, e.g., GPP(t) and Re(t). CCM gives a time-delay coordinate embedding of the system trajectories (fig. S3). The main algorithm is based on the nearest-neighbor forecasting (*51*), involving tracking the forward trajectory of nearby points in a lagged coordinate embedding. The embedding dimension (E) for a causal link, e.g., GPP(t)→Re(t) (the causes and effects hereafter all refer to this causal link), was determined by testing E from 2 to 10 dimensions based on the optimal cross-mapping skill lagged 1 day (figs. S14 and S15). In detail, Re(t) is used to predict GPP($t-1$) to prevent the overfitting of the cross-mapping between GPP(t) and Re(t) (*50*). E is the number of consecutive time-lag coordinates used for state-space reconstruction and can be viewed as the number of interacting variables of the underlying dynamics system for each time series. Note that $E+1$ is the minimum number of points needed for a bounding simplex in an E-dimensional space.

Quantification of causality strength between GPP and re via CCM

Taking time series of GPP and Re with length L, {*GPP*} = {GPP (1), GPP (2), ..., GPP(L)} and {*Re*} = {Re (1), Re (2), ..., Re(L)}, for example. Cross-mapping from Re to GPP begins with the lagged coordinate vectors, which is called a reconstructed manifold $\boldsymbol{M}_{\mathbf{Re}}$: $\boldsymbol{re}(\boldsymbol{t})$ = {$re_1(t)$, $re_2(t)$, $re_3(t)$, ..., $re_E(t)$} = {Re(t), *Re*($t-\tau$), *Re*($t-2\tau$), ..., *Re*[$t-(E-1)\tau$]} for $t = 1 + (E-1)\tau$ to L, where τ is the time delay, a time distance by which each delay vector $re_i(t)$ is shifted relative to the previous one. In other words, each vector in the reconstructed manifold corresponds to a value of the time series at a different time point, separated by the time delay τ. We used daily time distance both for time series GPP and Re because most time series were not overly sampled in time. The data used in our analysis were from June–August, so the longest data length was 92 in total without considering missing values. $\overline{\mathrm{GPP}}(t)|\boldsymbol{M}_{\mathbf{Re}}$ denotes the cross-mapped estimate of GPP(t) and is calculated as follows. First, locate the contemporaneous lagged coordinate vector on $\boldsymbol{M}_{\mathbf{Re}}$, $\boldsymbol{re}(\boldsymbol{t})$, and find its $E+1$ nearest neighbors. Second, denote the time indices of the $E+1$ nearest neighbors of $\boldsymbol{re}(\boldsymbol{t})$ by t_1, t_2, ..., t_{E+1} from the closest to farthest. The time indices correspond to the nearest neighbors to $\boldsymbol{re}(\boldsymbol{t})$ on $\boldsymbol{M}_{\mathbf{Re}}$ and are used to locate the neighbors in GPP to estimate GPP(t) from a locally weighted mean of the $E+1$ GPP(t_i) values

$$\overline{\mathrm{GPP}}(t) \mid M_{\mathrm{Re}} = \Sigma\omega_i \mathrm{GPP}(t_i) i = 1, 2, \ldots, E+1 \quad (2)$$

where ω_i is a weighting based on the Euclidean distance between $\boldsymbol{re}(\boldsymbol{t})$ and its ith nearest neighbor on $\boldsymbol{M}_{\mathbf{Re}}$. GPP($t_i$) is the contemporaneous value of GPP

$$\omega_i = u_i / \Sigma u_j j = 1, 2, \ldots, E+1 \quad (3)$$

where

$$u_i = \exp(-\|\boldsymbol{re}(\boldsymbol{t}), \boldsymbol{re}(\boldsymbol{t_i})\| / \|\boldsymbol{re}(\boldsymbol{t}), \boldsymbol{re}(\boldsymbol{t_1})\|) \quad (4)$$

$\|\boldsymbol{re}(\boldsymbol{m}), \boldsymbol{re}(\boldsymbol{k})\|$ is the Euclidean distance between two vectors in an E-dimensional space. That is, $\|\boldsymbol{re}(\boldsymbol{m}), \boldsymbol{re}(\boldsymbol{k})\| = (|re_1(m)\text{-}re_1(k)|^2 +$

$|re_2(m)\text{-}re_2(k)|^2 + \ldots + |re_E(m)\text{-}re_E(k)|^2)^{1/2}$. The cross-mapping skill

$$\rho = \mathrm{Cov}[GPP(t), \overline{GPP}(t) \,|\, M_{\mathrm{Re}}]/[\sqrt{\mathrm{Var}\ GPP(t)}\ \sqrt{\mathrm{Var}\ (\overline{GPP}(t)\,|\,M_{\mathrm{Re}})}] \quad (5)$$

Causation can happen with a lagged response (*37*). Several studies have found a time lag between GPP and Re with few days in forests (*52*, *53*). Therefore, we applied CCM with the highest cross-mapping skill, in detail, the causation between GPP(t) and $Re(t + k)$, where k is a time lag of 0, 1, 2, and 3 days. To precisely estimate the cross-mapping skill (ρ), we computed the average linkage strength from 100 random subsamples from the original time series.

A key property of CCM that distinguishes causation from simple correlation is convergence. The convergence was determined using different library sizes (L) subsampled randomly from Re(t). The minimum to the maximum range of L is E and the entire time series length. The significance test of CCM convergence is implemented by: (i) Fisher's Z test, to test whether the improvement in $\rho(L)$ is significant, i.e., whether $\rho(L_{\max})$ is significantly greater than $\rho(L_{\min})$; (ii) Kendall's τ test, to test whether $\rho(L)$ is significantly monotonically increasing. We admitted that GPP caused Re significantly when both tests were significant (*54*). The CCM analysis was conducted using the rEDM package in R (https://CRAN.R-project.org/package=rEDM). The results of CCM and the significance test of convergence are in tables S4 and S5. Notably, the use of the term "causal effect" in this study is determined by the converged cross-mapping skill ρ.

Redundancy analysis

We used RDA to examine the relationship between the predictors (table S2) and the enhanced causal effect strength of GPP on Re ($\Delta\rho_{\mathrm{GPP}\to\mathrm{Re}}$). RDA is a constrained ordination that extends regression analysis to multivariate response data. RDA maximizes the proportion of the interpreted response variables (*55*, *56*). The data were standardized to account for differences in scale and variance. First, a multivariate linear regression was computed between $\Delta\rho_{\mathrm{GPP}\to\mathrm{Re}}$ and the explanatory data to produce a matrix of fitted values. Second, principal components analysis of the fitted values produced canonical axes, which are linear combinations of the predictors.

The results show variations in the response and explanatory variables in a reduced dimensional space. In the plot, each point represents an observation, and the distance between the points indicates the degree of similarity or dissimilarity between the samples. The explanatory variables are represented as arrows, and the length and direction of the arrows indicate the strength and direction of their association with the response variable. We used "rda" for RDA in the vegan package in R (https://CRAN.R-project.org/package=vegan) for this analysis.

Relative importance method

We used a relative importance method to quantify the contribution of each predictor to the enhanced causal effect strength of GPP on Re, calculating the relative importance of the linear formula-based model with the factors in RDA analysis. The method estimates the total contribution of each predictor to the R^2 of the model, averaging over all possible orderings among regressors. The resulting values represent the average increase in R^2, so larger values indicate a larger contribution to the overall fit of the model. The sum of all the values is equal to the R^2 value of the full model. Therefore, the larger the sum of the values, the more the predictors collectively explain the variation in the response variable. This method can be a useful tool for providing insights into the relative importance of the predictors. We used metrics "lmg" in the "relaimpo" package in R (https://cran.r-project.org/web/packages/relaimpo/index.html).

CLM5 description

CLM5, the land component of the CESM2, is the latest version of CLM. CLM5 examines the physical, chemical, and biological processes of terrestrial ecosystems, which are closely linked to and influenced by climate on various spatial and temporal scales (*57*). CLM5 represents the achievement of the development and analysis of modern land models by the contributions from a diverse group of scientists from the Working Group on Chemistry Climate, Paleoclimate, Climate Change, and Land Ice, and so on and by the efforts from software engineers from diverse institutions like the Terrestrial Sciences Section and the Climate and Global Dynamics Division at the National Center for Atmospheric Research (NCAR). In CLM5, most major components have been updated, especially C and nitrogen cycling, river modeling, soil and plant hydrology, crop modeling, and snow density. CLM5 includes storage pools of NSCs used to meet excess demand for respiration during periods with low photosynthesis. The basis for the land cover description comes from MODIS land cover (MCD12Q1 v5.1), vegetation continuous fields (MOD44B v5.1), LAI (MCD15A2 v5), and albedo (MCD43B3 v5) products for the years 2001–2015 (*57*). In general, CLM5 simulates a range of land biogeophysical, biogeochemical, and landscape processes, including but not limited to processes of surface energy fluxes, soil and snow hydrology, stomatal physiology and photosynthesis, plant respiration, vegetation phenology, C and nitrogen allocation. CLM5 is publicly available through the Community Terrestrial System Model (CTSM) git repository (https://github.com/ESCOMP/ctsm). More information to access the documentation, tutorials, codes, model design and development, model output and diagnostics, and other previously released CLM model versions can be found on the CESM web page (www.cesm.ucar.edu/models/cesm2/land/). More details on the biogeophysical and biogeochemical parameterizations, numerical implementation, scientific descriptions, and operating instructions for CLM5 can refer to the full technical description of CLM5 (www.cesm.ucar.edu/models/cesm2/land/CLM50_Tech_Note.pdf).

CLM5 simulation and analysis

We performed model simulations with CLM5 offline of CESM2.1.2 using the meteorological forcing dataset CRUNCEP, the default forcing data in the Global Carbon Project TRENDY simulations (*58*), and the MsTMIP model intercomparison (*59*). CRUNCEP is a merged 6-hourly 0.5° global forcing product of the Climatic Research Unit Time-Series (CRU TS) version 3.24 monthly climate dataset (*60*) and the high-temporal resolution National Centers for Environmental Prediction (NCEP) reanalysis (*61*). The reanalysis data are used to generate diurnal and daily anomalies and add them to CRU TS monthly means. Temperature, precipitation, relative humidity, and cloudiness are based on CRU, while pressure, longwave radiation, and wind speed are directly obtained from NCEP. The version we used in this study is version 7. The dataset

CRUNCEPv7 is divided into three data streams: precipitation, solar, and a third category of variables. The third category includes pressure, temperature, wind, and humidity.

We conducted two simulations in CLM5, and the simulation period was from 2000 to 2016. One was driven by default meteorological forcing data, and the other by an increased temperature based on the default temperature forcing. The specific increased temperature was decided with the daily output temperature according to the former ambient simulation. That is, considering the weighting of summer daily temperatures, we added a weight-based temperature to the default temperature forcing for the Northern Hemisphere. The summer temperatures were increased by increments of 0.5°C, ranging from 0.5° to 4°C (fig. S16). The year 2016 was chosen as a heatwave year in the model because it was the year with the highest global average land and ocean surface temperature since 2020 (www.ncei.noaa.gov/access/monitoring/monthly-report/global/202013).

I2000Clm50BgcCru was set as the component set in the model simulations with prognostic vegetation state and active biogeochemistry, containing CLM with a data atmosphere model and stub ocean and sea-ice models. The initialization type of the CLM5 run was set as "startup." In a startup run, all components are initialized using baseline states, which are set independently by each component. Simulations were implemented at a resolution of 1.9° latitude by 2.5° longitude. In addition to the standard monthly output files, we added auxiliary history files to get the daily average output by adding hist_nhtfrq and set to −24 in the clm namelist. The June–August data were selected for further analysis.

CMIP6 ESMs descriptions and analyses

The most recent (sixth) Coupled Model Intercomparison Project (CMIP6) establishes standardized experimental protocols, forcing, and output, thereby promoting enhanced process comprehension in various domains, such as aerosols, clouds, impacts of volcanic eruptions on climate, and geoengineering (*62*). We used 11 comprehensive ESMs from CMIP6 in this study (table S3). The models were selected on the basis of the availability of some key variables in the climate-C cycle feedback, including variables such as GPP, heterotrophic respiration (rh), plant respiration (ra), vegetation C content (cVeg), air temperature (tas), soil C content (cSoil), and litter C content (cLitter). We selected one model per ESM institute because the models within each ESM institute had highly correlated results (*63*). Outputs from ESMs that contributed to CMIP6 are publicly available in a standardized format through the Earth System Grid Federation (ESGF) data replication centers (https://esgf-node.llnl.gov/search/cmip6/). Results from the historical experiments were analyzed. The historical simulations are forced by common datasets such as CO_2 and other greenhouse gas mixing ratios, land use change scenarios, and aerosol emissions that are largely based on time-dependent observational estimates. The simulation covers the period from 1850 to the end of 2014. The reported monthly value of GPP and Re (calculated as the sum of the heterotrophic and autotrophic respiration in ESMs) from 1980 to 2014 were used and resampled into 1° × 1° resolution. According to the latitude and longitude of the sites in 2003 heatwave events (table S1), we extracted the GPP and Re for each site in 11 ESMs. The GPP and Re were then used in CCM analysis to explore the uncertainty of the causal effect of GPP on Re among ESMs. For identifying the causal delays in GPP→Ra and GPP→Rh, we repeated CCM analysis by setting different cross-mapping time lags. The causal lag was determined at the optimal cross-mapping skill within one to three steps (unit: months). The results for each CMIP6 model were added as figs. S17 to S20. We used model outputs from the 1pctCO2-rad experiment in the C4MIP (*62*, *64*). The 1pctCO2-rad experiment was originally designed to estimate the carbon-climate feedback factor γ, which quantified the response of the C cycle to changes in physical climate (*64*, *65*). The "1pctCO2" represented 1% per year increasing atmospheric CO_2 concentration from the preindustrial level until quadrupling. The "rad" was the abbreviation of radiatively coupled simulations, in which radiative transfer processes in the atmosphere responded to elevated CO_2, but biogeochemical processes over land and ocean did not respond. The partial coupling scheme isolates responses of C cycle components to climate warming and CO_2 rising (*64*, *66*). On the basis of nine ESMs' simulations in the 1pctCO2-rad experiment (table S3), we analyzed how GPP and Re respond to summer temperature change.

Supplementary Materials

This PDF file includes:

Figs. S1 to S20
Tables S1 to S6
References

REFERENCES AND NOTES

1. P. Friedlingstein, M. O'Sullivan, M. W. Jones, R. M. Andrew, J. Hauck, A. Olsen, G. P. Peters, W. Peters, J. Pongratz, S. Sitch, C. L. Quéré, J. G. Canadell, P. Ciais, R. B. Jackson, S. Alin, L. E. O. C. Aragão, A. Arneth, V. Arora, N. R. Bates, M. Becker, A. Benoit-Cattin, H. C. Bittig, L. Bopp, S. Bultan, N. Chandra, F. Chevallier, L. P. Chini, W. Evans, L. Florentie, P. M. Forster, T. Gasser, M. Gehlen, D. Gilfillan, T. Gkritzalis, L. Gregor, N. Gruber, I. Harris, K. Hartung, V. Haverd, R. A. Houghton, T. Ilyina, A. K. Jain, E. Joetzjer, K. Kadono, E. Kato, V. Kitidis, J. I. Korsbakken, P. Landschützer, N. Lefèvre, A. Lenton, S. Lienert, Z. Liu, D. Lombardozzi, G. Marland, N. Metzl, D. R. Munro, J. E. M. S. Nabel, S. Nakaoka, Y. Niwa, K. O'Brien, T. Ono, P. I. Palmer, D. Pierrot, B. Poulter, L. Resplandy, E. Robertson, C. Rödenbeck, J. Schwinger, R. Séférian, I. Skjelvan, A. J. P. Smith, A. J. Sutton, T. Tanhua, P. P. Tans, H. Tian, B. Tilbrook, G. van der Werf, N. Vuichard, A. P. Walker, R. Wanninkhof, A. J. Watson, D. Willis, A. J. Wiltshire, W. Yuan, X. Yue, S. Zaehle, Global carbon budget 2020. *Earth Syst. Sci. Data* **12**, 3269–3340 (2020).
2. E. M. Fischer, R. Knutti, Anthropogenic contribution to global occurrence of heavy-precipitation and high-temperature extremes. *Nat. Clim. Chang.* **5**, 560–564 (2015).
3. N. Christidis, G. S. Jones, P. A. Stott, Dramatically increasing chance of extremely hot summers since the 2003 European heatwave. *Nat. Clim. Chang.* **5**, 46–50 (2015).
4. J. Zhu, S. Wang, E. M. Fischer, Increased occurrence of day–night hot extremes in a warming climate. *Climate Dynam.* **59**, 1297–1307 (2022).
5. E. M. Fischer, S. Sippel, R. Knutti, Increasing probability of record-shattering climate extremes. *Nat. Clim. Chang.* **11**, 689–695 (2021).
6. A. C. Bennett, S. K. Arndt, L. T. Bennett, J. Knauer, J. Beringer, A. Griebel, N. Hinko-Najera, M. J. Liddell, D. Metzen, E. Pendall, R. P. Silberstein, T. J. Wardlaw, W. Woodgate, V. Haverd, Thermal optima of gross primary productivity are closely aligned with mean air temperatures across Australian wooded ecosystems. *Glob. Chang. Biol.* **27**, 4727–4744 (2021).
7. M. Huang, S. Piao, P. Ciais, J. Peñuelas, X. Wang, T. F. Keenan, S. Peng, J. A. Berry, K. Wang, J. Mao, R. Alkama, A. Cescatti, M. Cuntz, H. De Deurwaerder, M. Gao, Y. He, Y. Liu, Y. Luo, R. B. Myneni, S. Niu, X. Shi, W. Yuan, H. Verbeeck, T. Wang, J. Wu, I. A. Janssens, Air temperature optima of vegetation productivity across global biomes. *Nat. Ecol. Evol.* **3**, 772–779 (2019).
8. B. E. Medlyn, E. Dreyer, D. Ellsworth, M. Forstreuter, P. C. Harley, M. U. F. Kirschbaum, X. Le Roux, P. Montpied, J. Strassemeyer, A. Walcroft, K. Wang, D. Loustau, Temperature response of parameters of a biochemically based model of photosynthesis. II. A review of experimental data. *Plant Cell Environ.* **25**, 1167–1179 (2002).
9. Ü. Niinemets, Global-scale climatic controls of leaf dry mass per area, density, and thickness in trees and shrubs. *Ecology* **82**, 453–469 (2001).

10. K. B. Wilson, D. D. Baldocchi, P. J. Hanson, Leaf age affects the seasonal pattern of photosynthetic capacity and net ecosystem exchange of carbon in a deciduous forest. *Plant Cell Environ.* **24**, 571–583 (2001).
11. C. Grossiord, T. N. Buckley, L. A. Cernusak, K. A. Novick, B. Poulter, R. T. W. Siegwolf, J. S. Sperry, N. G. McDowell, Plant responses to rising vapor pressure deficit. *New Phytol.* **226**, 1550–1566 (2020).
12. M. Sprintsin, J. M. Chen, A. Desai, C. M. Gough, Evaluation of leaf-to-canopy upscaling methodologies against carbon flux data in North America. *J. Geophys. Res.* **117**, G01023 (2012).
13. P. De Frenne, J. Lenoir, M. Luoto, B. R. Scheffers, F. Zellweger, J. Aalto, M. B. Ashcroft, D. M. Christiansen, G. Decocq, K. De Pauw, S. Govaert, C. Greiser, E. Gril, A. Hampe, T. Jucker, D. H. Klinges, I. A. Koelemeijer, J. J. Lembrechts, R. Marrec, C. Meeussen, J. Ogée, V. Tyystjärvi, P. Vangansbeke, K. Hylander, Forest microclimates and climate change: Importance, drivers and future research agenda. *Glob. Chang. Biol.* **27**, 2279–2297 (2021).
14. T. F. Keenan, J. Gray, M. A. Friedl, M. Toomey, G. Bohrer, D. Y. Hollinger, J. W. Munger, J. O'Keefe, H. P. Schmid, I. S. Wing, B. Yang, A. D. Richardson, Net carbon uptake has increased through warming-induced changes in temperate forest phenology. *Nat. Clim. Chang.* **4**, 598–604 (2014).
15. A. S. A. Johnston, A. Meade, J. Ardö, N. Arriga, A. Black, P. D. Blanken, D. Bonal, C. Brümmer, A. Cescatti, J. Dušek, A. Graf, B. Gioli, I. Goded, C. M. Gough, H. Ikawa, R. Jassal, H. Kobayashi, V. Magliulo, G. Manca, L. Montagnani, F. E. Moyano, J. E. Olesen, T. Sachs, C. Shao, T. Tagesson, G. Wohlfahrt, S. Wolf, W. Woodgate, A. Varlagin, C. Venditti, Temperature thresholds of ecosystem respiration at a global scale. *Nat. Ecol. Evol.* **5**, 487–494 (2021).
16. K. A. Duffy, C. R. Schwalm, V. L. Arcus, G. W. Koch, L. L. Liang, L. A. Schipper, How close are we to the temperature tipping point of the terrestrial biosphere? *Sci. Adv.* **7**, eaay1052 (2021).
17. C. Rödenbeck, S. Zaehle, R. Keeling, M. Heimann, The European carbon cycle response to heat and drought as seen from atmospheric CO_2 data for 1999-2018. *Phil. Trans. R. Soc. B.* **375**, 20190506 (2020).
18. J. von Buttlar, J. Zscheischler, A. Rammig, S. Sippel, M. Reichstein, A. Knohl, M. Jung, O. Menzer, M. A. Arain, N. Buchmann, A. Cescatti, D. Gianelle, G. Kiely, B. E. Law, V. Magliulo, H. Margolis, H. McCaughey, L. Merbold, M. Migliavacca, L. Montagnani, W. Oechel, M. Pavelka, M. Peichl, S. Rambal, A. Raschi, R. L. Scott, F. P. Vaccari, E. van Gorsel, A. Varlagin, G. Wohlfahrt, M. D. Mahecha, Impacts of droughts and extreme-temperature events on gross primary production and ecosystem respiration: A systematic assessment across ecosystems and climate zones. *Biogeosciences* **15**, 1293–1318 (2018).
19. P. Ciais, M. Reichstein, N. Viovy, A. Granier, J. Ogée, V. Allard, M. Aubinet, N. Buchmann, C. Bernhofer, A. Carrara, F. Chevallier, N. De Noblet, A. D. Friend, P. Friedlingstein, T. Grünwald, B. Heinesch, P. Keronen, A. Knohl, G. Krinner, D. Loustau, G. Manca, G. Matteucci, F. Miglietta, J. M. Ourcival, D. Papale, K. Pilegaard, S. Rambal, G. Seufert, J. F. Soussana, M. J. Sanz, E. D. Schulze, T. Vesala, R. Valentini, Europe-wide reduction in primary productivity caused by the heat and drought in 2003. *Nature* **437**, 529–533 (2005).
20. M. Reichstein, P. Ciais, D. Papale, R. Valentini, S. Running, N. Viovy, W. Cramer, A. Granier, J. Ogée, V. Allard, M. Aubinet, C. Bernhofer, N. Buchmann, A. Carrara, T. Grünwald, M. Heimann, B. Heinesch, A. Knohl, W. Kutsch, D. Loustau, G. Manca, G. Matteucci, F. Miglietta, J. M. Ourcival, K. Pilegaard, J. Pumpanen, S. Rambal, S. Schaphoff, G. Seufert, J.-F. Soussana, M.-J. Sanz, T. Vesala, M. Zhao, Reduction of ecosystem productivity and respiration during the European summer 2003 climate anomaly: A joint flux tower, remote sensing and modelling analysis. *Glob. Chang. Biol.* **13**, 634–651 (2007).
21. L. Qu, J. Chen, G. Dong, S. Jiang, L. Li, J. Guo, C. Shao, Heat waves reduce ecosystem carbon sink strength in a Eurasian meadow steppe. *Environ. Res.* **144**, 39–48 (2016).
22. Y. Du, R. Lu, J. Xia, Impacts of global environmental change drivers on non-structural carbohydrates in terrestrial plants. *Funct. Ecol.* **34**, 1525–1536 (2020).
23. S. Sevanto, N. G. Mcdowell, L. T. Dickman, R. Pangle, W. T. Pockman, How do trees die? A test of the hydraulic failure and carbon starvation hypotheses. *Plant Cell Environ.* **37**, 153–161 (2014).
24. A. D. Collins, M. G. Ryan, H. D. Adams, L. T. Dickman, N. Garcia-Forner, C. Grossiord, H. H. Powers, S. Sevanto, N. G. McDowell, Foliar respiration is related to photosynthetic, growth and carbohydrate response to experimental drought and elevated temperature. *Plant Cell Environ.* **44**, 3853–3865 (2021).
25. S. Jones, L. Rowland, P. Cox, D. Hemming, A. Wiltshire, K. Williams, N. C. Parazoo, J. Liu, A. C. L. da Costa, P. Meir, M. Mencuccini, A. B. Harper, The impact of a simple representation of non-structural carbohydrates on the simulated response of tropical forests to drought. *Biogeosciences* **17**, 3589–3612 (2020).
26. S. Wan, J. Xia, W. Liu, S. Niu, Photosynthetic overcompensation under nocturnal warming enhances grassland carbon sequestration. *Ecology* **90**, 2700–2710 (2009).
27. J. Xia, J. Chen, S. Piao, P. Ciais, Y. Luo, S. Wan, Terrestrial carbon cycle affected by non-uniform climate warming. *Nat. Geosci.* **7**, 173–180 (2014).
28. M. J. Paul, C. H. Foyer, Sink regulation of photosynthesis. *J. Exp. Bot.* **52**, 1383–1400 (2001).
29. Y. Salmon, A. Lintunen, A. Dayet, T. Chan, R. Dewar, T. Vesala, T. Hölttä, Leaf carbon and water status control stomatal and nonstomatal limitations of photosynthesis in trees. *New Phytol.* **226**, 690–703 (2020).
30. R. L. Thompson, G. Broquet, C. Gerbig, T. Koch, M. Lang, G. Monteil, S. Munassar, A. Nickless, M. Scholze, M. Ramonet, U. Karstens, E. van Schaik, Z. Wu, C. Rödenbeck, Changes in net ecosystem exchange over Europe during the 2018 drought based on atmospheric observations. *Phil. Trans. R Soc. B.* **375**, 20190512 (2020).
31. M. Reichstein, D. Papale, R. Valentini, M. Aubinet, C. Bernhofer, A. Knohl, T. Laurila, A. Lindroth, E. Moors, K. Pilegaard, G. Seufert, Determinants of terrestrial ecosystem carbon balance inferred from European eddy covariance flux sites. *Geophys. Res. Lett.* **34**, L01402 (2007).
32. J. Runge, S. Bathiany, E. Bollt, G. Camps-Valls, D. Coumou, E. Deyle, C. Glymour, M. Kretschmer, M. D. Mahecha, J. Muñoz-Marí, E. H. van Nes, J. Peters, R. Quax, M. Reichstein, M. Scheffer, B. Schölkopf, P. Spirtes, G. Sugihara, J. Sun, K. Zhang, J. Zscheischler, Inferring causation from time series in Earth system sciences. *Nat. Commun.* **10**, 2553 (2019).
33. G. Sugihara, R. May, H. Ye, C.-H. Hsieh, E. Deyle, M. Fogarty, S. Munch, Detecting causality in complex ecosystems. *Science* **338**, 496–500 (2012).
34. U. Triacca, Is Granger causality analysis appropriate to investigate the relationship between atmospheric concentration of carbon dioxide and global surface air temperature? *Theor. Appl. Climatol.* **81**, 133–135 (2005).
35. J. Runge, V. Petoukhov, J. F. Donges, J. Hlinka, N. Jajcay, M. Vejmelka, D. Hartman, N. Marwan, M. Paluš, J. Kurths, Identifying causal gateways and mediators in complex spatio-temporal systems. *Nat. Commun.* **6**, 8502 (2015).
36. F. Takens, Detecting strange attractors in turbulence, in *Dynamical Systems and Turbulence, Warwick 1980. Lecture Notes in Mathematics*, D. Rand, L. S. Young, Eds. (Springer Berlin Heidelberg, Berlin, Heidelberg, 1981), vol. 898, pp. 366–381.
37. E. H. van Nes, M. Scheffer, V. Brovkin, T. M. Lenton, H. Ye, E. Deyle, G. Sugihara, Causal feedbacks in climate change. *Nat. Clim. Chang.* **5**, 445–448 (2015).
38. C.-W. Chang, H. Ye, T. Miki, E. R. Deyle, S. Souissi, O. Anneville, R. Adrian, Y.-R. Chiang, S. Ichise, M. Kumagai, S. S. Matsuzaki, F.-K. Shiah, J.-T. Wu, C.-H. Hsieh, G. Sugihara, Long-term warming destabilizes aquatic ecosystems through weakening biodiversity-mediated causal networks. *Glob. Chang. Biol.* **26**, 6413–6423 (2020).
39. A. Koutsodendris, V. Dakos, W. J. Fletcher, M. Knipping, U. Kotthoff, A. M. Milner, U. C. Müller, S. Kaboth-Bahr, O. A. Kern, L. Kolb, P. Vakhrameeva, S. Wulf, K. Christanis, G. Schmiedl, J. Pross, Atmospheric CO_2 forcing on Mediterranean biomes during the past 500 kyrs. *Nat. Commun.* **14**, 1664 (2023).
40. M. Ushio, C.-H. Hsieh, R. Masuda, E. R. Deyle, H. Ye, C.-W. Chang, G. Sugihara, M. Kondoh, Fluctuating interaction network and time-varying stability of a natural fish community. *Nature* **554**, 360–363 (2018).
41. T. Hölttä, A. Lintunen, T. Chan, A. Mäkelä, E. Nikinmaa, A steady-state stomatal model of balanced leaf gas exchange, hydraulics and maximal source–sink flux. *Tree Physiol.* **37**, 851–868 (2017).
42. R. Dewar, T. Hölttä, Y. Salmon, Exploring optimal stomatal control under alternative hypotheses for the regulation of plant sources and sinks. *New Phytol.* **233**, 639–654 (2022).
43. A. Potkay, X. Feng, Do stomata optimize turgor-driven growth? A new framework for integrating stomata response with whole-plant hydraulics and carbon balance. *New Phytol.* **238**, 506–528 (2023).
44. N. G. McDowell, R. A. Fisher, C. Xu, J. C. Domec, T. Hölttä, D. S. Mackay, J. S. Sperry, A. Boutz, L. Dickman, N. Gehres, J. M. Limousin, A. Macalady, J. Martínez-Vilalta, M. Mencuccini, J. A. Plaut, J. Ogée, R. E. Pangle, D. P. Rasse, M. G. Ryan, S. Sevanto, R. H. Waring, A. P. Williams, E. A. Yepez, W. T. Pockman, Evaluating theories of drought-induced vegetation mortality using a multimodel–experiment framework. *New Phytol.* **200**, 304–321 (2013).
45. A. Cabon, S. A. Kannenberg, A. Arain, F. Babst, D. Baldocchi, S. Belmecheri, N. Delpierre, R. Guerrieri, J. T. Maxwell, S. McKenzie, F. C. Meinzer, D. J. P. Moore, C. Pappas, A. V. Rocha, P. Szejner, M. Ueyama, D. Ulrich, C. Vincke, S. L. Voelker, J. Wei, D. Woodruff, W. R. L. Anderegg, Cross-biome synthesis of source versus sink limits to tree growth. *Science* **376**, 758–761 (2022).
46. P. A. Stott, D. A. Stone, M. R. Allen, Human contribution to the European heatwave of 2003. *Nature* **432**, 610–614 (2004).
47. M. Aubinet, A. Grelle, A. Ibrom, Ü. Rannik, J. Moncrieff, T. Foken, A. S. Kowalski, P. H. Martin, P. Berbigier, C. Bernhofer, R. Clement, J. Elbers, A. Granier, T. Grünwald, K. Morgenstern, K. Pilegaard, C. Rebmann, W. Snijders, R. Valentini, T. Vesala, Estimates of the annual net carbon and water exchange of forests: The EUROFLUX methodology. *Adv Ecol. Res.* **30**, 113–175 (1999).
48. Drought 2018 Team and ICOS Ecosystem Thematic Centre: Drought-2018 ecosystem eddy covariance flux product for 52 stations in FLUXNET-Archive format (2020); https://doi.org/10.18160/YVR0-4898.

49. G. Pastorello, C. Trotta, E. Canfora, H. Chu, D. Christianson, Y.-W. Cheah, C. Poindexter, J. Chen, A. Elbashandy, M. Humphrey, P. Isaac, D. Polidori, M. Reichstein, A. Ribeca, C. van Ingen, N. Vuichard, L. Zhang, B. Amiro, C. Ammann, M. A. Arain, J. Ardö, T. Arkebauer, S. K. Arndt, N. Arriga, M. Aubinet, M. Aurela, D. Baldocchi, A. Barr, E. Beamesderfer, L. B. Marchesini, O. Bergeron, J. Beringer, C. Bernhofer, D. Berveiller, D. Billesbach, T. A. Black, P. D. Blanken, G. Bohrer, J. Boike, P. V. Bolstad, D. Bonal, J.-M. Bonnefond, D. R. Bowling, R. Bracho, J. Brodeur, C. Brümmer, N. Buchmann, B. Burban, S. P. Burns, P. Buysse, P. Cale, M. Cavagna, P. Cellier, S. Chen, I. Chini, T. R. Christensen, J. Cleverly, A. Collalti, C. Consalvo, B. D. Cook, D. Cook, C. Coursolle, E. Cremonese, P. S. Curtis, E. D'Andrea, H. da Rocha, X. Dai, K. J. Davis, B. De Cinti, A. de Grandcourt, A. De Ligne, R. C. De Oliveira, N. Delpierre, A. R. Desai, C. M. Di Bella, P. di Tommasi, H. Dolman, F. Domingo, G. Dong, S. Dore, P. Duce, E. Dufrêne, A. Dunn, J. Dušek, D. Eamus, U. Eichelmann, H. A. M. ElKhidir, W. Eugster, C. M. Ewenz, B. Ewers, D. Famulari, S. Fares, I. Feigenwinter, A. Feitz, R. Fensholt, G. Filippa, M. Fischer, J. Frank, M. Galvagno, M. Gharun, D. Gianelle, B. Gielen, B. Gioli, A. Gitelson, I. Goded, M. Goeckede, A. H. Goldstein, C. M. Gough, M. L. Goulden, A. Graf, A. Griebel, C. Gruening, T. Grünwald, A. Hammerle, S. Han, X. Han, B. U. Hansen, C. Hanson, J. Hatakka, Y. He, M. Hehn, B. Heinesch, N. Hinko-Najera, L. Hörtnagl, L. Hutley, A. Ibrom, H. Ikawa, M. Jackowicz-Korczynski, D. Janouš, W. Jans, R. Jassal, S. Jiang, T. Kato, M. Khomik, J. Klatt, A. Knohl, S. Knox, H. Kobayashi, G. Koerber, O. Kolle, Y. Kosugi, A. Kotani, A. Kowalski, B. Kruijt, J. Kurbatova, W. L. Kutsch, H. Kwon, S. Launiainen, T. Laurila, B. Law, R. Leuning, Y. Li, M. Liddell, J.-M. Limousin, M. Lion, A. J. Liska, A. Lohila, A. López-Ballesteros, E. López-Blanco, B. Loubet, D. Loustau, A. Lucas-Moffat, J. Lüers, S. Ma, C. Macfarlane, V. Magliulo, R. Maier, I. Mammarella, G. Manca, B. Marcolla, H. A. Margolis, S. Marras, W. Massman, M. Mastepanov, R. Matamala, J. H. Matthes, F. Mazzenga, H. McCaughey, I. McHugh, A. M. S. McMillan, L. Merbold, W. Meyer, T. Meyers, S. D. Miller, S. Minerbi, U. Moderow, R. K. Monson, L. Montagnani, C. E. Moore, E. Moors, V. Moreaux, C. Moureaux, J. W. Munger, T. Nakai, J. Neirynck, Z. Nesic, G. Nicolini, A. Noormets, M. Northwood, M. Nosetto, Y. Nouvellon, K. Novick, W. Oechel, J. E. Olesen, J.-M. Ourcival, S. A. Papuga, F.-J. Parmentier, E. Paul-Limoges, M. Pavelka, M. Peichl, E. Pendall, R. P. Phillips, K. Pilegaard, N. Pirk, G. Posse, T. Powell, H. Prasse, S. M. Prober, S. Rambal, Ü. Rannik, N. Raz-Yaseef, C. Rebmann, D. Reed, V. R. de Dios, N. Restrepo-Coupe, B. R. Reverter, M. Roland, S. Sabbatini, T. Sachs, S. R. Saleska, E. P. Sánchez-Cañete, Z. M. Sanchez-Mejia, H. P. Schmid, M. Schmidt, K. Schneider, F. Schrader, I. Schroder, R. L. Scott, P. Sedlák, P. Serrano-Ortíz, C. Shao, P. Shi, I. Shironya, L. Siebicke, L. Šigut, R. Silberstein, C. Sirca, D. Spano, R. Steinbrecher, R. M. Stevens, C. Sturtevant, A. Suyker, T. Tagesson, S. Takanashi, Y. Tang, N. Tapper, J. Thom, M. Tomassucci, J.-P. Tuovinen, S. Urbanski, R. Valentini, M. van der Molen, E. van Gorsel, K. van Huissteden, A. Varlagin, J. Verfaillie, T. Vesala, C. Vincke, D. Vitale, N. Vygodskaya, J. P. Walker, E. Walter-Shea, H. Wang, R. Weber, S. Westermann, C. Wille, S. Wofsy, G. Wohlfahrt, S. Wolf, W. Woodgate, Y. Li, R. Zampedri, J. Zhang, G. Zhou, D. Zona, D. Agarwal, S. Biraud, M. Torn, D. Papale, The FLUXNET2015 dataset and the ONEFlux processing pipeline for eddy covariance data. *Sci. Data* **7**, 225 (2020).
50. E. R. Deyle, R. M. May, S. B. Munch, G. Sugihara, Tracking and forecasting ecosystem interactions in real time. *Proc. R. Soc. B* **283**, 20152258 (2016).
51. G. Sugihara, R. M. May, Nonlinear forecasting as a way of distinguishing chaos from measurement error in time series. *Nature* **344**, 734–741 (1990).
52. M. Migliavacca, M. Reichstein, A. D. Richardson, R. Colombo, M. A. Sutton, G. Lasslop, E. Tomelleri, G. Wohlfahrt, N. Carvalhais, A. Cescatti, M. D. Mahecha, L. Montagnani, D. Papale, S. Zaehle, A. Arain, A. Arneth, T. A. Black, A. Carrara, S. Dore, D. Gianelle, C. Helfter, D. Hollinger, W. L. Kutsch, P. M. Lafleur, Y. Nouvellon, C. Rebmann, H. R. Da Rocha, M. Rodeghiero, O. Roupsard, M.-T. Sebastià, G. Seufert, J.-F. Soussana, M. K. Van Der Molen, Semiempirical modeling of abiotic and biotic factors controlling ecosystem respiration across eddy covariance sites. *Glob. Chang. Biol.* **17**, 390–409 (2011).
53. F. R. Moyano, W. L. Kutsch, C. Rebmann, Soil respiration fluxes in relation to photosynthetic activity in broad-leaf and needle-leaf forest stands. *Agric. For. Meteorol.* **148**, 135–143 (2008).
54. C.-W. Chang, M. Ushio, C.-H. Hsieh, Empirical dynamic modeling for beginners. *Ecol. Res.* **32**, 785–796 (2017).
55. C. Rellstab, F. Gugerli, A. J. Eckert, A. M. Hancock, R. Holderegger, A practical guide to environmental association analysis in landscape genomics. *Mol. Ecol.* **24**, 4348–4370 (2015).
56. T. Capblancq, K. Luu, M. G. B. Blum, E. Bazin, Evaluation of redundancy analysis to identify signatures of local adaptation. *Mol. Ecol. Resour.* **18**, 1223–1233 (2018).
57. D. M. Lawrence, R. A. Fisher, C. D. Koven, K. W. Oleson, S. C. Swenson, G. Bonan, N. Collier, B. Ghimire, L. van Kampenhout, D. Kennedy, E. Kluzek, P. J. Lawrence, F. Li, H. Li, D. Lombardozzi, W. J. Riley, W. J. Sacks, M. Shi, M. Vertenstein, W. R. Wieder, C. Xu, A. A. Ali, A. M. Badger, G. Bisht, M. van den Broeke, M. A. Brunke, S. P. Burns, J. Buzan, M. Clark, A. Craig, K. Dahlin, B. Drewniak, J. B. Fisher, M. Flanner, A. M. Fox, P. Gentine, F. Hoffman, G. Keppel-Aleks, R. Knox, S. Kumar, J. Lenaerts, L. R. Leung, W. H. Lipscomb, Y. Lu, A. Pandey, J. D. Pelletier, J. Perket, J. T. Randerson, D. M. Ricciuto, B. M. Sanderson, A. Slater, Z. M. Subin, J. Tang, R. Q. Thomas, M. V. Martin, X. Zeng, The community land model version 5: Description of new features, benchmarking, and impact of forcing uncertainty. *J. Adv. Model. Earth Syst.* **11**, 4245–4287 (2019).
58. C. Le Quéré, R. M. Andrew, P. Friedlingstein, S. Sitch, J. Pongratz, A. C. Manning, J. I. Korsbakken, G. P. Peters, J. G. Canadell, R. B. Jackson, T. A. Boden, P. P. Tans, O. D. Andrews, V. K. Arora, D. C. E. Bakker, L. Barbero, M. Becker, R. A. Betts, L. Bopp, F. Chevallier, L. P. Chini, P. Ciais, C. E. Cosca, J. Cross, K. Currie, T. Gasser, I. Harris, J. Hauck, V. Haverd, R. A. Houghton, C. W. Hunt, G. Hurtt, T. Ilyina, A. K. Jain, E. Kato, M. Kautz, R. F. Keeling, K. K. Goldewijk, A. Körtzinger, P. Landschützer, N. Lefèvre, A. Lenton, S. Lienert, I. Lima, D. Lombardozzi, N. Metzl, F. Millero, P. M. S. Monteiro, D. R. Munro, J. E. M. S. Nabel, S.-I. Nakaoka, Y. Nojiri, X. A. Padin, A. Peregon, B. Pfeil, D. Pierrot, B. Poulter, G. Rehder, J. Reimer, C. Rödenbeck, J. Schwinger, R. Séférian, I. Skjelvan, B. D. Stocker, H. Tian, B. Tilbrook, F. N. Tubiello, I. T. van der Laan-Luijkx, G. R. van der Werf, S. van Heuven, N. Viovy, N. Vuichard, A. P. Walker, A. J. Watson, A. J. Wiltshire, S. Zaehle, D. Zhu, Global carbon budget 2017. *Earth Syst. Sci. Data* **10**, 405–448 (2018).
59. D. N. Huntzinger, C. Schwalm, A. M. Michalak, K. Schaefer, A. W. King, Y. Wei, A. Jacobson, S. Liu, R. B. Cook, W. M. Post, G. Berthier, D. Hayes, M. Huang, A. Ito, H. Lei, C. Lu, J. Mao, C. H. Peng, S. Peng, B. Poulter, D. Riccuito, X. Shi, H. Tian, W. Wang, N. Zeng, F. Zhao, Q. Zhu, The North American carbon program multi-scale synthesis and terrestrial model intercomparison project – part 1: Overview and experimental design. *Geosci. Model Dev.* **6**, 2121–2133 (2013).
60. I. Harris, P. D. Jones, T. J. Osborn, D. H. Lister, Updated high-resolution grids of monthly climatic observations—The CRU TS3.10 Dataset. *Int. J. Climatol.* **34**, 623–642 (2014).
61. E. Kalnay, M. Kanamitsu, R. Kistler, W. Collins, D. Deaven, L. Gandin, M. Iredell, S. Saha, G. White, J. Woollen, Y. Zhu, M. Chelliah, W. Ebisuzaki, W. Higgins, J. Janowiak, K. C. Mo, C. Ropelewski, J. Wang, A. Leetmaa, R. Reynolds, R. Jenne, D. Joseph, The NCEP/NCAR 40-year reanalysis project. *Bull. Am. Meteorol. Soc.* **77**, 437–471 (1996).
62. V. Eyring, S. Bony, G. A. Meehl, C. A. Senior, B. Stevens, R. J. Stouffer, K. E. Taylor, Overview of the Coupled Model Intercomparison Project Phase 6 (CMIP6) experimental design and organization. *Geosci. Model Dev.* **9**, 1937–1958 (2016).
63. K. E. O. Todd-Brown, J. T. Randerson, F. Hopkins, V. Arora, T. Hajima, C. Jones, E. Shevliakova, J. Tjiputra, E. Volodin, T. Wu, Q. Zhang, S. D. Allison, Changes in soil organic carbon storage predicted by Earth system models during the 21st century. *Biogeosciences* **11**, 2341–2356 (2014).
64. C. D. Jones, V. Arora, P. Friedlingstein, L. Bopp, V. Brovkin, J. Dunne, H. Graven, F. Hoffman, T. Ilyina, J. G. John, M. Jung, M. Kawamiya, C. Koven, J. Pongratz, T. Raddatz, J. T. Randerson, S. Zaehle, C4MIP–The Coupled Climate–Carbon Cycle Model Intercomparison Project: Experimental protocol for CMIP6. *Geosci. Model Dev.* **9**, 2853–2880 (2016).
65. V. K. Arora, A. Katavouta, R. G. Williams, C. D. Jones, V. Brovkin, P. Friedlingstein, J. Schwinger, L. Bopp, O. Boucher, P. Cadule, M. A. Chamberlain, J. R. Christian, C. Delire, R. A. Fisher, T. Hajima, T. Ilyina, E. Joetzjer, M. Kawamiya, C. D. Koven, J. P. Krasting, R. M. Law, D. M. Lawrence, A. Lenton, K. Lindsay, J. Pongratz, T. Raddatz, R. Séférian, K. Tachiiri, J. F. Tjiputra, A. Wiltshire, T. Wu, T. Ziehn, Carbon–concentration and carbon–climate feedbacks in CMIP6 models and their comparison to CMIP5 models. *Biogeosciences* **17**, 4173–4222 (2020).
66. P. Friedlingstein, P. Cox, R. Betts, L. Bopp, W. von Bloh, V. Brovkin, P. Cadule, S. Doney, M. Eby, I. Fung, G. Bala, J. John, C. Jones, F. Joos, T. Kato, M. Kawamiya, W. Knorr, K. Lindsay, H. D. Matthews, T. Raddatz, P. Rayner, C. Reick, E. Roeckner, K.-G. Schnitzler, R. Schnur, K. Strassmann, A. J. Weaver, C. Yoshikawa, N. Zeng, Climate–carbon cycle feedback analysis: Results from the C4MIP model intercomparison. *J. Climate* **19**, 3337–3353 (2006).
67. R. M. Law, T. Ziehn, R. J. Matear, A. Lenton, M. A. Chamberlain, L. E. Stevens, Y. Wang, J. Srbinovsky, D. Bi, H. Yan, P. F. Vohralik, The carbon cycle in the Australian Community Climate and Earth System Simulator (ACCESS-ESM1) – Part 1: Model description and pre-industrial simulation. *Geosci. Model Dev.* **10**, 2567–2590 (2017).
68. T. Wu, Y. Lu, Y. Fang, X. Xin, L. Li, W. Li, W. Jie, J. Zhang, Y. Liu, L. Zhang, F. Zhang, Y. Zhang, F. Wu, J. Li, M. Chu, Z. Wang, X. Shi, X. Liu, M. Wei, A. Huang, Y. Zhang, X. Liu, The Beijing Climate Center Climate System Model (BCC-CSM): The main progress from CMIP5 to CMIP6. *Geosci. Model Dev.* **12**, 1573–1600 (2019).
69. N. C. Swart, J. N. S. Cole, V. V. Kharin, M. Lazare, J. F. Scinocca, N. P. Gillett, J. Anstey, V. Arora, J. R. Christian, S. Hanna, Y. Jiao, W. G. Lee, F. Majaess, O. A. Saenko, C. Seiler, C. Seinen, A. Shao, M. Sigmond, L. Solheim, K. von Salzen, D. Yang, B. Winter, The Canadian Earth System Model version 5 (CanESM5.0.3). *Geosci. Model Dev.* **12**, 4823–4873 (2019).
70. T. Lovato, D. Peano, M. Butenschön, S. Materia, D. Iovino, E. Scoccimarro, P. G. Fogli, A. Cherchi, A. Bellucci, S. Gualdi, S. Masina, A. Navarra, CMIP6 simulations with the CMCC Earth System Model (CMCC-ESM2). *J. Adv. Model. Earth Syst.* **14**, e2021MS002814 (2022).
71. R. Séférian, P. Nabat, M. Michou, D. Saint-Martin, A. Voldoire, J. Colin, B. Decharme, C. Delire, S. Berthet, M. Chevallier, S. Sénési, L. Franchisteguy, J. Vial, M. Mallet, E. Joetzjer, O. Geoffroy, J.-F. Guérémy, M.-P. Moine, R. Msadek, A. Ribes, M. Rocher, R. Roehrig, D. Salas-y-Mélia, E. Sanchez, L. Terray, S. Valcke, R. Waldman, O. Aumont, L. Bopp, J. Deshayes, C. Éthé, G. Madec, Evaluation of CNRM Earth System model, CNRM-ESM2-1: Role of Earth system

processes in present-day and future climate. *J. Adv. Model. Earth Syst.* **11**, 4182–4227 (2019).

72. R. Döscher, M. Acosta, A. Alessandri, P. Anthoni, T. Arsouze, T. Bergman, R. Bernardello, S. Boussetta, L.-P. Caron, G. Carver, M. Castrillo, F. Catalano, I. Cvijanovic, P. Davini, E. Dekker, F. J. Doblas-Reyes, D. Docquier, P. Echevarria, U. Fladrich, R. Fuentes-Franco, M. Gröger, J. V. Hardenberg, J. Hieronymus, M. P. Karami, J.-P. Keskinen, T. Koenigk, R. Makkonen, F. Massonnet, M. Ménégoz, P. A. Miller, E. Moreno-Chamarro, L. Nieradzik, T. van Noije, P. Nolan, D. O'Donnell, P. Ollinaho, G. van den Oord, P. Ortega, O. T. Prims, A. Ramos, T. Reerink, C. Rousset, Y. Ruprich-Robert, P. Le Sager, T. Schmith, R. Schrödner, F. Serva, V. Sicardi, M. S. Madsen, B. Smith, T. Tian, E. Tourigny, P. Uotila, M. Vancoppenolle, S. Wang, D. Wårlind, U. Willén, K. Wyser, S. Yang, X. Yepes-Arbós, Q. Zhang, The EC-Earth3 Earth system model for the Coupled Model Intercomparison Project 6. *Geosci. Model Dev.* **15**, 2973–3020 (2022).
73. O. Boucher, J. Servonnat, A. L. Albright, O. Aumont, Y. Balkanski, V. Bastrikov, S. Bekki, R. Bonnet, S. Bony, L. Bopp, P. Braconnot, P. Brockmann, P. Cadule, A. Caubel, F. Cheruy, F. Codron, A. Cozic, D. Cugnet, F. D'Andrea, P. Davini, C. de Lavergne, S. Denvil, J. Deshayes, M. Devilliers, A. Ducharne, J.-L. Dufresne, E. Dupont, C. Éthé, L. Fairhead, L. Falletti, S. Flavoni, M.-A. Foujols, S. Gardoll, G. Gastineau, J. Ghattas, J.-Y. Grandpeix, B. Guenet, E. G. Lionel, E. Guilyardi, M. Guimberteau, D. Hauglustaine, F. Hourdin, A. Idelkadi, S. Joussaume, M. Kageyama, M. Khodri, G. Krinner, N. Lebas, G. Levavasseur, C. Lévy, L. Li, F. Lott, T. Lurton, S. Luyssaert, G. Madec, J.-B. Madeleine, F. Maignan, M. Marchand, O. Marti, L. Mellul, Y. Meurdesoif, J. Mignot, I. Musat, C. Ottlé, P. Peylin, Y. Planton, J. Polcher, C. Rio, N. Rochetin, C. Rousset, P. Sepulchre, A. Sima, D. Swingedouw, R. Thiéblemont, A. K. Traore, M. Vancoppenolle, J. Vial, J. Vialard, N. Viovy, N. Vuichard, Presentation and evaluation of the IPSL-CM6A-LR climate model. *J. Adv. Model. Earth Syst.* **12**, e2019MS002010 (2020).
74. T. Hajima, M. Watanabe, A. Yamamoto, H. Tatebe, M. A. Noguchi, M. Abe, R. Ohgaito, A. Ito, D. Yamazaki, H. Okajima, A. Ito, K. Takata, K. Ogochi, S. Watanabe, M. Kawamiya, Development of the MIROC-ES2L Earth system model and the evaluation of biogeochemical processes and feedbacks. *Geosci. Model Dev.* **13**, 2197–2244 (2020).
75. T. Mauritsen, J. Bader, T. Becker, J. Behrens, M. Bittner, R. Brokopf, V. Brovkin, M. Claussen, T. Crueger, M. Esch, I. Fast, S. Fiedler, D. Fläschner, V. Gayler, M. Giorgetta, D. S. Goll, H. Haak, S. Hagemann, C. Hedemann, C. Hohenegger, T. Ilyina, T. Jahns, D. Jimenéz-de-la-Cuesta, J. Jungclaus, T. Kleinen, S. Kloster, D. Kracher, S. Kinne, D. Kleberg, G. Lasslop, L. Kornblueh, J. Marotzke, D. Matei, K. Meraner, U. Mikolajewicz, K. Modali, B. Möbis, W. A. Müller, J. E. M. S. Nabel, C. C. W. Nam, D. Notz, S.-S. Nyawira, H. Paulsen, K. Peters, R. Pincus, H. Pohlmann, J. Pongratz, M. Popp, T. Jürgen, S. Rast, R. Redler, C. H. Reick, T. Rohrschneider, V. Schemann, H. Schmidt, R. Schnur, U. Schulzweida, K. D. Six, L. Stein, I. Stemmler, B. Stevens, J.-S. von Storch, F. Tian, A. Voigt, P. Vrese, K.-H. Wieners, S. Wilkenskjeld, A. Winkler, E. Roeckner, Developments in the MPI-M Earth System Model version 1.2 (MPI-ESM1.2) and Its Response to Increasing CO_2. *J. Adv. Model. Earth Syst.* **11**, 998–1038 (2019).
76. S. Yukimoto, H. Kawai, T. Koshiro, N. Oshima, K. Yoshida, S. Urakawa, H. Tsujino, M. Deushi, T. Tanaka, M. Hosaka, S. Yabu, H. Yoshimura, E. Shindo, R. Mizuta, A. Obata, Y. Adachi, M. Ishii, The Meteorological Research Institute Earth System Model version 2.0, MRI-ESM2.0: Description and basic evaluation of the physical component. *J. Meteorol. Soc. Jpn.* **97**, 931–965 (2019).
77. Ø. Seland, M. Bentsen, D. Olivié, T. Toniazzo, A. Gjermundsen, L. S. Graff, J. B. Debernard, A. K. Gupta, Y.-C. He, A. Kirkevåg, J. Schwinger, J. Tjiputra, K. S. Aas, I. Bethke, Y. Fan, J. Griesfeller, A. Grini, C. Guo, M. Ilicak, I. H. H. Karset, O. Landgren, J. Liakka, K. O. Moseid, A. Nummelin, C. Spensberger, H. Tang, Z. Zhang, C. Heinze, T. Iversen, M. Schulz, Overview of the Norwegian Earth System Model (NorESM2) and key climate response of CMIP6 DECK, historical, and scenario simulations. *Geosci. Model Dev.* **13**, 6165–6200 (2020).
78. A. A. Sellar, C. G. Jones, J. P. Mulcahy, Y. Tang, A. Yool, A. Wiltshire, F. M. O'Connor, M. Stringer, R. Hill, J. Palmieri, S. Woodward, L. Mora, T. Kuhlbrodt, S. T. Rumbold, D. I. Kelley, R. Ellis, C. E. Johnson, J. Walton, N. L. Abraham, M. B. Andrews, T. Andrews, A. T. Archibald, S. Berthou, E. Burke, E. Blockley, K. Carslaw, M. Dalvi, J. Edwards, G. A. Folberth, N. Gedney, P. T. Griffiths, A. B. Harper, M. A. Hendry, A. J. Hewitt, B. Johnson, A. Jones, C. D. Jones, J. Keeble, S. Liddicoat, O. Morgenstern, R. J. Parker, V. Predoi, E. Robertson, A. Siahaan, R. S. Smith, R. Swaminathan, M. T. Woodhouse, G. Zeng, M. Zerroukat, UKESM1: Description and evaluation of the U.K. Earth System Model. *J. Adv. Model. Earth Syst.* **11**, 4513–4558 (2019).

Acknowledgments: We are grateful to Z. Tu for their insightful comments on our manuscript. We acknowledge the ICOS Infrastructure for support in collecting and processing the eddy covariance data for 2018. We thank the European Research projects and individual scientists who decided to share their measurements openly for providing standard and high-quality data processing and data sharing tools. The eddy covariance data processing and harmonization were carried out by the AmeriFlux Management Project, the European Fluxes Database, and the ICOS Ecosystem Thematic Centre. We acknowledge FLUXNET for the work on the open datasets. The CESM project is supported primarily by the National Science Foundation (NSF). Administration of the CESM is maintained by the Climate and Global Dynamics Laboratory (CGD) at the NCAR. We also acknowledge the World Climate Research Programme, which, through its Working Group on Coupled Modelling, coordinated and promoted CMIP6. We would like to thank the climate modeling groups for producing and making model output available, the ESGF for archiving the data and providing access, and the multiple funding agencies who support CMIP6 and ESGF. **Funding:** This work is financially supported by the National Key R&D Program of China (2022YFF0802104) and the Shanghai Pilot Program for Basic Research (TQ20220102). **Author contributions:** All co-authors have made substantial contributions to this work. J.X. and J.P. conceived this study. J.X., S.N., and Y.L. contributed to the formulation of the overarching research aim. J.P. and E.C. contributed to the visualizations. E.C., Y.D., N.W., and J.W. contributed to the review and editing. J.Z. contributed to the methodology of CLM5 offline configurations. J.P. interpreted the results and wrote the original manuscript with input from all co-authors. **Competing interests:** The authors declare that they have no competing interests. **Data and materials availability:** All data needed to evaluate the conclusions in the paper are present in the paper and/or the Supplementary Materials. A frozen version of the code that performed the main causal analysis is uploaded to the Zenodo archive with DOI: 10.5281/zenodo.8248269.

Submitted 9 May 2023
Accepted 21 September 2023
Published 25 October 2023
10.1126/sciadv.adi6395

ScienceAdvances

Enhanced causal effect of ecosystem photosynthesis on respiration during heatwaves

Jiaye Ping, Erqian Cui, Ying Du, Ning Wei, Jian Zhou, Jing Wang, Shuli Niu, Yiqi Luo, and Jianyang Xia

Sci. Adv. **9** (43), eadi6395. DOI: 10.1126/sciadv.adi6395

Science Advances (ISSN 2375-2548) is published by the American Association for the Advancement of Science. 1200 New York Avenue NW, Washington, DC 20005. The title *Science Advances* is a registered trademark of AAAS.